OPEN ACCESS



The RESOLVE and ECO G3 Initiative: Drivers of H1 Content and X-Ray Emission in Galaxy Groups

Zackary L. Hutchens^{1,2}, Sheila J. Kannappan¹, Kelley M. Hess^{3,4,5}, Andrew J. Baker^{6,7}, Ming Sun⁸, Derrick S. Carr¹, Kathleen D. Eckert¹, and David V. Stark^{9,10}

Department of Physics & Astronomy, University of North Carolina at Chapel Hill, 120 E. Cameron Ave., Chapel Hill, NC 27599, USA; zhutchen@live.unc.edu

Department of Physics & Astronomy, University of North Carolina Asheville, 1 University Heights, Asheville, NC 28804, USA

Department of Space, Earth and Environment, Chalmers University of Technology, Onsala Space Observatory, 43992 Onsala, Sweden

ASTRON, The Netherlands Institute for Radio Astronomy, Postbus 2, 7990 AA, Dwingeloo, The Netherlands

Institute de Astrofísica de Andalucía (CSIC), Glorieta de la Astronomía, 18008 Granada, Spain

Department of Physics and Astronomy, Rutgers, The State University of New Jersey, 136 Frelinghuysen Road, Piscataway, NJ 08854-8019, USA

Department of Physics and Astronomy, University of the Western Cape, Robert Sobukwe Road, Bellville 7535, South Africa

Department of Physics and Astronomy, The University of Alabama in Huntsville, 301 Sparkman Drive, Huntsville, AL 35899, USA

Space Telescope Science Institute, 3700 San Martin Dr., Baltimore, MD 21218, USA

William H. Miller III Department of Physics and Astronomy, Johns Hopkins University, Baltimore, MD 21218, USA

Received 2024 June 13; revised 2025 March 7; accepted 2025 March 14; published 2025 May 27

Abstract

Adding to the RESOLVE and ECO Gas in Galaxy Groups (G3) initiative, we examine possible drivers of group-integrated H I-to-halo mass ratios ($M_{\rm HI,grp}/M_{\rm halo}$) and group X-ray emission, including group halo mass ($M_{\rm halo}$), virialization as probed by crossing time ($t_{\rm cross}$), presence of active galactic nuclei (AGN), and group-integrated fractional stellar mass growth rate (FSMGR_{grp}). G3 groups span $M_{\rm halo} = 10^{11} - 10^{14.5} \, M_{\odot}$ with comprehensive H I gas and AGN information, which we combine with X-ray stacking of ROSAT All-Sky data. We detect hot gas emission exceeding AGN and X-ray binary backgrounds confidently for $M_{\rm halo} = 10^{12.6} - 10^{14} \, M_{\odot}$ and unambiguously for $M_{\rm halo} > 10^{14} \, M_{\odot}$, reflecting an inverse dependence of $M_{\rm HI,grp}/M_{\rm halo}$ and hot gas emission on halo mass. At fixed halo mass, $M_{\rm HI,grp}/M_{\rm halo}$ transitions to greater spread below $t_{\rm cross} \sim 2$ Gyr. Dividing groups across this transition, lower- $t_{\rm cross}$ groups show elevated X-ray emission compared to higher- $t_{\rm cross}$ groups for $M_{\rm halo} > 10^{13.3} \, M_{\odot}$, but this trend reverses for $M_{\rm halo} = 10^{12.6} - 10^{13.3} \, M_{\odot}$. Additionally, AGN-hosting halos below $M_{\rm halo} \sim 10^{12.1} \, M_{\odot}$ exhibit a broad, ~ 0.25 dex deep valley in $M_{\rm HI,grp}/M_{\rm halo}$ compared to non-AGN-hosting halos with correspondingly reduced FSMGR_{grp}. When diluted by non-AGN-hosting halos, this valley becomes shallower and narrower, falling roughly between $M_{\rm halo} = 10^{11.5} \, M_{\odot}$ and $M_{\rm halo} = 10^{12.1} \, M_{\odot}$ in the overall $M_{\rm HI,grp}/M_{\rm halo}$ vs. $M_{\rm halo}$ relation. We may also detect a second, less easily interpreted valley at $M_{\rm halo} \sim 10^{13} \, M_{\odot}$. Neither valley matches theoretical predictions of a deeper valley located at or above $M_{\rm halo} = 10^{12.1} \, M_{\odot}$.

Unified Astronomy Thesaurus concepts: Galaxies (573); Galaxy dark matter halos (1880); X-ray astronomy (1810); Active galactic nuclei (16)

1. Introduction

Neutral atomic hydrogen (H I) is the primary mass component of the interstellar medium in galaxies like the Milky Way (P. M. Kalberla & J. Kerp 2009). Given its role in fueling star formation (SF) and active galactic nucleus (AGN) activity, HI is a crucial ingredient in galaxy evolution. To investigate how environment affects the HI content of galaxies and groups, recent observations and models have addressed the group HIhalo mass relation (here the $M_{\rm HI,grp}$ - $M_{\rm halo}$ relation, where "halo" refers to the shared group halo; if a halo contains only one galaxy, we call it an $N_{\rm galaxies} = 1$ group). The $M_{\rm HI,grp} - M_{\rm halo}$ relation describes the total HI mass contained by a halo as a function of dark matter halo mass, and as such, its shape and scatter reflect cosmic gas accretion, assembly history, and feedback from AGN and SF (A. Obuljen et al. 2019). Previous $z\sim0$ observations of this relation indicate (i) a transition to a shallower slope above $M_{\rm halo}\sim10^{11.5}\,M_{\odot}$, corresponding to the peak integrated H I-to-halo mass ratio, and (ii) a substantial scatter of at least ~ 0.3 dex, suggesting that secondary factors

Original content from this work may be used under the terms of the Creative Commons Attribution 4.0 licence. Any further distribution of this work must maintain attribution to the author(s) and the title of the work, journal citation and DOI.

regulate group H I content at fixed halo mass (K. D. Eckert et al. 2017; A. Obuljen et al. 2019; H. Guo et al. 2020; A. Dev et al. 2023; Z. L. Hutchens et al. 2023; M. Saraf et al. 2024). In this paper, we investigate some of these secondary factors—virialization state, SF, and AGN content—and relate them to both H I content and hot gas traced by X-ray emission.

In theoretical models, virial shocks are believed to be the primary halo mass-dependent mechanism of gas heating in groups. In the model of A. Dekel & Y. Birnboim (2006, hereafter DB06), the onset of virial shock heating within $0.1R_{\rm vir}$ occurs at the same $M_{\rm halo} \sim 10^{11.5} \, M_{\odot}$ scale where the $M_{\rm HI,grp} M_{\rm halo}$ relation transitions in slope. This "gas-richness threshold scale" (as named by S. J. Kannappan et al. 2009, due to the preponderance of H I gas-dominated galaxies below it; see also A. Dekel & J. Silk 1986; D. R. Garnett 2002; J. J. Dalcanton et al. 2004; S. J. Kannappan 2004; S. J. Kannappan et al. 2013) corresponds approximately to a stellar mass for the central galaxy of $M_* \sim 10^{9.5} M_{\odot}$ via the stellar mass-halo mass relation (P. S. Behroozi et al. 2010). Below the corresponding halo mass, theory predicts efficient gas cooling (Y. Birnboim & A. Dekel 2003; D. Kereš et al. 2005; A. Dekel & Y. Birnboim 2006; D. Nelson et al. 2013), as evidenced by the rapid refueling and stellar mass growth of galaxies in this regime (S. J. Kannappan et al. 2013). Slow, inefficient accretion is

expected above the higher $M_{\rm halo} \sim 10^{12.1}\,M_{\odot}$ "bimodality scale" (corresponding to central galaxy $M_{*} \sim 10^{10.5}\,M_{\odot}$), where the A. Dekel & Y. Birnboim (2006) model predicts full halo gas heating (see also, e.g., J. M. Gabor & R. Davé 2015) and where observations show changes in galaxy morphology and stellar populations (G. Kauffmann et al. 2003). These critical transitions in galaxy properties suggest that halo-driven gas heating may suppress galaxy HI content via stripping and starvation. While hot gas halos have been detected in high-mass groups (M. Sun et al. 2009; H. Eckmiller et al. 2011; M. E. Anderson et al. 2015; A. Jakobs et al. 2018) and down to $M_{\rm halo} = 10^{11} \, M_{\odot}$ (D.-W. Kim & G. Fabbiano 2013; A. D. Goulding et al. 2016; D. A. Forbes et al. 2017; Á. Bogdán & M. Vogelsberger 2022; Y. Zhang et al. 2024), these studies have generally not examined the interdependence of hot gas and H I gas as a function of halo mass or other group properties, such as virialization state. Prior work connecting group hot and cold gas content has largely focused on single groups or small samples of compact groups (e.g., J. Rasmussen et al. 2012; T. D. Desjardins et al. 2014; E. O'Sullivan et al. 2018).

The dynamical state of a group may affect gas heating at fixed halo mass. As the dynamical evolution of a group progresses, simulations suggest that major and minor mergers may result in shocks that heat, and generate turbulence within, the intragroup medium (M. Sinha & K. Holley-Bockelmann 2009; X. Shi et al. 2020). In a small sample of NGC groups, E. M. Wilcots (2009) found that dynamically evolved groups host predominantly hot and ionized gas content, whereas dynamically young groups are more H I-rich. The importance of group assembly in regulating H I content is demonstrated in the results of K. M. Hess & E. M. Wilcots (2013), who found that H I-rich galaxies preferentially reside on the outskirts of groups and that the infall of HI-rich satellites is crucial to replenish H_I in group halos. Additionally, in a study of 172 Sloan Digital Sky Survey (SDSS) groups with halo masses $M_{\rm halo} \gtrsim 10^{13} \, M_{\odot}$, M. Ai & M. Zhu (2018) showed that group H I-to-halo mass ratios decrease with decreasing crossing time, corresponding to lower- t_{cross} states. Further analysis is needed to assess whether the relationship between group HI content and crossing time extends to lower-mass halos, and if so, what physical processes drive the relationship.

SF and AGN are also expected to affect group H I content at fixed halo mass, via feedback within halos. In semi-analytic models, K. D. Eckert et al. (2017) found that ratios of hot halo gas to cold galaxy gas become widely varying in the $M_{\rm halo}\sim 10^{11.4}-10^{12.1}\,M_{\odot}$ regime, likely reflecting a transition in the dominant feedback source from SF to AGN. In lowermass halos. SF feedback is expected from supernovae or the winds of young, massive stars; in higher-mass halos, AGN feedback is expected to heat or expel halo gas, thereby suppressing SF or gas cooling (R. S. Somerville et al. 2008; M. Gaspari et al. 2014; D. Fielding et al. 2017). AGN feedback in dwarf galaxies may also lead to H I suppression in low-mass halos, as seen in the model of G. Dashyan et al. (2018) and observations of J. D. Bradford et al. (2018), in which dwarf galaxies are defined by virial mass $M_{\rm vir} < 10^{11} M_{\odot}$ and stellar mass $M_* < 10^{9.5}$, respectively. Without special attention to dwarf AGN, recent theoretical models of the $M_{\rm HI,grp}$ – $M_{\rm halo}$ relation have predicted an AGN-driven "dip" at $M_{\rm halo} \sim 10^{12.1} - 10^{12.5} \, M_{\odot}$ (H.-S. Kim et al. 2017; C. Baugh et al. 2019; G. Chauhan et al. 2020). This dip has evaded direct

observation, possibly being eroded by observational systematics (G. Chauhan et al. 2021). A fresh look with attention to dwarf AGN is warranted, given dramatic improvements in their detection (M. S. Polimera et al. 2022; M. Mezcua & H. D. Sánchez 2024).

In this paper, we ask three questions about the drivers of group H I and hot gas:

- 1. How do group cold gas and X-ray emission depend on halo mass?
- 2. How do group cold gas and X-ray emission depend on virialization state at fixed halo mass?
- 3. How do group cold gas and X-ray emission depend on AGN prevalence and recent (~last Gyr) SF history at fixed halo mass?

To answer these three questions, we combine archival ROSAT All-Sky Survey (RASS) data (W. Voges 1993) with data from the Gas in Galaxy Groups (G3) initiative, a spin-off of the highly complete and volume-limited REsolved Spectroscopy Of a Local VolumE (RESOLVE; S. J. Kannappan & L. H. Wei 2008) and Environmental COntext (ECO; A. J. Moffett et al. 2015) surveys. RESOLVE and ECO provide a complete census of a combined \sim 456,300 Mpc⁻³ volume of the $z \sim 0$ Universe, with comprehensive H I mass, SF history, and AGN data extending down to the dwarf regime, as needed to answer these questions. In G3 Paper I (Z. L. Hutchens et al. 2023, hereafter H23), we constructed a group catalog for these surveys with optimal purity, completeness, and halo mass estimation. By stacking RASS imaging of G3 groups, we can analyze X-ray emission in relation to group H I content, virialization state, SF, and AGN activity.

This paper proceeds as follows: We describe the RASS data and the optical group catalogs for the G3 initiative in Section 2. We describe our methods for reprocessing and stacking RASS imaging in Section 3. We outline our results in Section 4 and discuss their implications in Section 5. Finally, we summarize our findings in Section 6. Throughout this work, we adopt a Λ CDM cosmology with $H_0 = 70 \, \mathrm{km \, s^{-1} \, Mpc^{-1}}$, $\Omega_{m,0} = 0.3$, and $\Omega_{\Lambda,0} = 0.7$.

2. Data

2.1. RESOLVE and ECO Gas in Galaxy Groups

In this section, we describe RESOLVE, ECO, and the G3 group catalogs.

2.1.1. RESOLVE

RESOLVE is a highly complete, volume- and luminosity-limited census of stellar, gas, and dynamical mass in $\sim\!53,\!000\,\mathrm{Mpc^3}$ of the local Universe (S. J. Kannappan & L. H. Wei 2008). It contains $\sim\!1600$ galaxies in two equatorial strips, RESOLVE-A (131°.25 < R.A. < 236°.25, 0° < decl. < 5°) and RESOLVE-B (330° < R.A. < 45°, -1°.25 < decl. < +1°.25). Both RESOLVE-A and RESOLVE-B are limited by $4500 < cz_{\rm grp} < 7000$, where $cz_{\rm grp}$ is the Local Group –corrected recessional velocity of the galaxy's group, described further in Section 2.1.3. RESOLVE-A is complete to $M_r = -17.33$ in the SDSS r band, while RESOLVE-B (overlapping the deeper Stripe 82 region) is complete to

¹¹ For both RESOLVE and ECO, our reported R.A. and decl. ranges are in the J2000 coordinate frame.

 $M_r = -17.0$ (K. D. Eckert et al. 2015, 2016). Thus, defining dwarfs as galaxies with $M_r \geqslant -19.5$, RESOLVE is dwarf dominated. RESOLVE data products include custom-reprocessed UV-near-IR photometry, as well as stellar masses and SF history data derived from stellar population synthesis modeling (K. D. Eckert et al. 2015, based on S. J. Kannappan et al. 2013).

RESOLVE also provides a comprehensive atomic gas census that offers HI detections or strong upper limits $(1.4 \, M_{\rm HI}/M_* \lesssim 0.05 - 0.1)$ for ~94% of galaxies (D. V. Stark et al. 2016, updated in H23). These measurements were derived from targeted Arecibo and Green Bank Telescope observations (D. V. Stark et al. 2016) and supplemented by archival data from ALFALFA (M. P. Haynes et al. 2011, 2018) and C. M. Springob et al. (2005). Cases of confusion were identified automatically by searching for companions in existing redshift surveys, and deconfusion was attempted as outlined by D. V. Stark et al. (2016). A majority (81%) of RESOLVE's HI gas masses are based on such clean HI detections, successfully deconfused detections, or strong upper limits, which we treat as best estimates of HI mass. For the remaining 19% of cases (missing 21 cm observations, weak upper limits, or confused detections that could not be deconfused), H23 estimated H1 gas masses using the photometric gas fraction technique (S. J. Kannappan 2004; K. D. Eckert et al. 2015), as constrained by weak upper limits or confused total fluxes when available.

In addition to photometry and HI mass information, the present work uses RESOLVE's AGN inventory (M. S. Polimera et al. 2025, in preparation). One of the advantages of our analysis is that this AGN catalog provides a uniform and unusually complete selection of low-mass galaxy AGN, found using both optical emission-line diagnostics (which reveal the new "SF-AGN" class of low-metallicity/star-forming AGN found by M. S. Polimera et al. 2022 and additional dwarf AGN identified by the loosened BPT diagnostic of G. Stasińska et al. 2006) and mid-IR color diagnostics (which are sensitive to a complementary set of dwarf AGN candidates; S. Satyapal et al. 2018; M. S. Polimera et al. 2025, in preparation; see Section 4.3 regarding reliability concerns for mid-IR AGN). Additionally, the catalog provides cross-matched data on previously identified X-ray AGN (P. Ranalli et al. 2003), broad-line AGN (H.-Y. Liu et al. 2019), and other AGN crossmatched from the literature (M. P. Véron-Cetty & P. Véron 2006; E. W. Flesch 2015).

2.1.2. ECO

The ECO (A. J. Moffett et al. 2015; updated by H23) catalog surrounds RESOLVE-A in a \sim 10 times larger volume of \sim 440,000 Mpc⁻³. ECO's larger volume supports the smaller but superior RESOLVE survey by enabling larger-sample studies of environment and assessment of cosmic variance. The ECO volume is defined by $3000 < cz_{\rm grp} < 7000$, $130.05 < {\rm R.A.} < 237.45$, and $-1^{\circ} < {\rm decl.} < 49.85$. ECO reaches the same luminosity completeness floor as RESOLVE-A ($M_r = -17.33$) but is purely archival, except where new observations were incorporated via its overlap with RESOLVE-A. All ECO data products, including photometry and H I mass information, were processed using RESOLVE pipelines to improve quality and harmonize the two surveys. Like RESOLVE, ECO offers a uniform and unusually complete AGN catalog based on multiple optical emission-line diagnostics and mid-IR colors,

which also provides cross-matched data on known broad-line AGN, X-ray AGN, and other AGN from the literature (see Section 2.1.1).

Additionally, ECO contains a flux-limited census of H I gas composed of inherited RESOLVE-A observations and crossmatched sources from ALFALFA (M. P. Haynes et al. 2018), including new upper limits and confusion flags (see H23). As for RESOLVE, H23 computed the best H1 mass estimate for each ECO galaxy by combining clean H I detections, upper limits, confused fluxes, and constrained photometric gas fraction estimates (see Section 2.1.1), with the exception that deconfusion was not attempted for confused ECO galaxies outside RESOLVE-A. For these confused sources in ECO, HI mass estimates are always from photometric gas fractions constrained by confused fluxes. For the entire ECO survey, 45% of our best HI mass estimates are based on clean detections, strong upper limits, or (in the RESOLVE-A overlap region only) deconfused observations; the remaining 55% are photometric gas fraction estimates for galaxies with weak upper limits, confused 21 cm observations, or missing 21 cm observations.

2.1.3. G3 Groups

The group catalogs used for our X-ray stacking analysis were created by H23 using the G3 group finder, whose four-step algorithm offers improved completeness and halo mass recovery compared to friends-of-friends group finding. For the analysis in this paper, we combine the G3 group catalogs from RESOLVE-B and ECO (where the latter includes RESOLVE-A). We selected groups whose most luminous galaxies (which we refer to as "central galaxies") are above the survey luminosity floors and whose average group redshifts fall within the respective survey redshift ranges of $3000 < cz_{grp}$ [km s⁻¹] < 7000 (ECO) and $4500 < cz_{\rm grp}$ [km s⁻¹] < 7000 (RESOLVE-B). The selection on $cz_{\rm grp}$ mitigates the clipping of groups when galaxy peculiar velocities would otherwise have extended beyond the survey redshift limits. The resulting selection yields 6949 groups with halo masses spanning $M_{\rm halo} = 10^{11} - 10^{14.5} \, M_{\odot}$, consisting of 6038 $N_{\text{galaxies}} = \hat{1}$ groups, 512 galaxy pairs, and 399 groups with $\geqslant 3$ galaxies. We exclude the Coma Cluster from our stacking analyses, as its intense X-ray emission makes it an outlier among our other massive groups, so our final sample consists of 910 groups/pairs and 6038 $N_{\text{galaxies}} = 1$ groups.

2.1.4. G3 Group Properties

In our analysis in Section 4, we use RESOLVE and ECO data to compute four main group properties needed to answer the questions introduced in Section 1:

1. Group halo mass M_{halo} : Group halo masses for G3 groups were derived in H23 using abundance matching (A. V. Kravtsov et al. 2004; M. R. Blanton & A. A. Berlind 2007). With this technique, H23 built a one-to-one monotonic relationship between group halo mass and group-integrated r-band luminosity using the theoretical halo mass function of J. Tinker et al. (2008). The derived halo masses and radii assume a mean background overdensity of $\Delta_{\text{vir}} = 337$, representing the boundary of the virialized halo (e.g., E. D'Onghia et al. 2005). Compared to the common alternatives of 200 or 500, our halo masses scale as $M_{337} = 0.85 M_{200}$ and $M_{337} = 1.1 M_{500}$. Since halo radii $R_{\text{halo}} \propto M_{\text{halo}}^{1/3}$, our virial

- radii scale as $R_{337} = 0.95R_{200}$ and $R_{337} = 1.04R_{500}$ (see W. Hu & A. V. Kravtsov 2003).
- 2. Group-integrated H I mass $M_{\rm HI,grp}$: As in H23, we compute group-integrated H I mass by summing galactic H I mass estimates for group members. ¹² These H I mass estimates are a combined data set of clean H I detections, strong upper limits, deconfused H I detections, and estimates from photometric gas fractions (possibly constrained by upper limit/confused flux data; see H23 for a description of how this method incorporates upper limit and confused data). For $N_{\rm galaxies} = 1$ groups, $M_{\rm HI,grp}$ is the galaxy $M_{\rm HI}$. In Section 4, we derive errors on median $M_{\rm HI,grp}/M_{\rm halo}$ values using bootstrapping with 5000 resamples.
- 3. Group-integrated fractional stellar mass growth rate FSMGR_{grp}: The galaxy fractional stellar mass growth rate (FSMGR) is the ratio of stellar mass formed within the past Gyr, $M_{*,1 \text{ Gyr}}$, to the preexisting stellar mass formed over all previous Gyr, $M_{*,preex}$ (S. J. Kannappan et al. 2013). We calculate FSMGR using the spectral distribution (SED) modeling energy code S. J. Kannappan et al. (2013; based on S. J. Kannappan & E. Gawiser 2007), which uses our custom near-UV-IR photometry (see K. D. Eckert et al. 2015; A. J. Moffett et al. 2015; H23). We prefer FSMGR as an SF metric over the common alternative, specific star formation rate (sSFR = SFR/ M_*), because FSMGR is better suited to probe high fractional growth regimes of SF: an FSMGR can reach arbitrarily large values, whereas an sSFR approaches an asymptotic maximum as recent stellar mass growth increases, contributing to both SFR and M_* . We calculate group-integrated FSMGR as FSMGR_{grp} = $(\sum M_{*,1 \text{ Gyr}})/(\sum M_{*,\text{preex}})$, where these sums are computed over all group members. For $N_{\text{galaxies}} = 1$ groups, FSMGR_{grp} is the galaxy FSMGR. In Section 4, we derive errors on median FSMGR_{grp} values using bootstrapping with 5000 resamples.
- 4. Group crossing time t_{cross} : To assess virialization state, we use the crossing time $t_{\rm cross} = \langle R_{\rm proj,gal} \rangle / \langle |v_{\rm proj,gal}| \rangle$ (H. J. Rood & J. R. Dickel 1978; see also H. C. Ferguson & A. Sandage 1990; P. Firth et al. 2006), where $\langle R_{\text{proj,gal}} \rangle$ and $\langle |v_{\text{proj,gal}}| \rangle$ are the mean projected transverse distance and mean absolute line-of-sight velocity, respectively, for grouped galaxies relative to their average group center (see Section 2.2). This metric represents the mean time for a galaxy to traverse the group and is usually expressed relative to the age of the Universe (P. Hickson et al. 1992). A system of galaxies freely expanding with the Hubble flow will have a crossing time comparable to the age of the Universe, whereas if the crossing time is short compared to the age of the Universe, then the group is a bound, virialized system (J. R. Gott & E. L. Turner 1977). Unlike other virialization metrics (e.g., the Dressler-Shectman statistic; A. Dressler & S. A. Shectman 1988), t_{cross} can be

calculated for all $N_{\rm galaxies} \geqslant 2$ groups. However, we note that $t_{\rm cross}$ is a noisy metric of virialization, being both subject to observational projection effects and sensitive to abrupt changes due to merging (e.g., when the smallest $R_{\rm proj,gal}$ values are eliminated after a merger).

2.2. ROSAT All-Sky Survey Data

We use archival X-ray imaging from RASS (W. Voges 1993; S. Snowden et al. 1994). RASS was conducted in scanning mode using ROSAT's Position Sensitive Proportional Counters (PSPC) to observe 1378 6.4 × 6.4 fields in three energy bands. We obtained broadband ($\sim 0.1-2.3 \text{ keV}$, PSPC channels 11–235) and hard-band ($\sim 0.44-2.04$ keV, PSPC channels 52-201) photon count maps, exposure maps, and background count maps via the High Energy Astrophysics Science Research Center (HEASARC). 13 Since we obtained the most significant results in the RASS hard band, we do not show broadband stacking results in this paper. For each G3 group, we extracted custom-mosaicked maps at the average group center (see H23), using the Python library reproject to ensure flux conservation. While the location of the brightest cluster galaxy (BCG) is a common alternative to the average group center, R. A. Skibba et al. (2011) showed that 25%–40% of BCGs in halos of mass $M_{\rm halo} > 10^{12.1} \, M_{\odot}$ are not actually the galaxies with the lowest specific potential energies in their halos. Moreover, G. Gozaliasl et al. (2019) measured considerable $0.2R_{\rm vir}$ - $0.3R_{\rm vir}$ offsets between BCGs and X-ray centroids of groups, which depend on both halo mass and magnitude gap (probing virialization state). These findings suggest that the position of the BCG is not the optimal location to stack X-ray emission in groups.

3. RASS Image Processing and Stacking

In this section, we outline our four-step strategy for reprocessing and stacking RASS data: (1) image masking to remove extraneous point and diffuse sources, (2) image scaling and cropping to enable stacking on a common scale, (3) group image stacking, and (4) random image stacking.

3.1. Source Masking

We implemented source masking to exclude nearby extraneous sources and to separate point-source (including unresolved galaxy) emission from extended emission within our groups. To do so, we applied an iterative sigma-clipping Python algorithm from the photutils (A. M. Price-Whelan et al. 2022) to detect and then mask any $\geq 5\sigma$ sources lying outside the group virial radius in each image. This code creates a segmentation map in which sources may have arbitrary geometries, allowing us to mask both point and extended sources. In addition, we masked sources listed in the Second ROSAT X-ray Source (2RXS) catalog (T. Boller et al. 2016). To select sources for masking from 2RXS, we excluded 2RXS objects with detection likelihood EXI $ML \leq 9$, which lowers the 2RXS spurious source fraction to \sim 5% (see T. Boller et al. 2016). We also excluded nine 2RXS sources that cross-matched to RESOLVE or ECO galaxies within 6" (the median effective radius of RESOLVE/ECO galaxies), as for some analyses we choose to include galactic emission and

¹² Given the sizes of the Arecibo and GBT beams, our galactic H I masses may sometimes include intragroup gas and/or gas-rich, optically undetected satellite galaxies. However, given that intragroup H I outweighs galactic H I by at most a factor of 1.5–2 even in intragroup-dominant systems (W. Van Driel et al. 1992; S. Borthakur et al. 2015), we do not expect a significant contribution from intragroup H I affecting our results. In fact, our group H I masses are largely consistent with those of H. Guo et al. (2020), who measured the H I-halo mass relation using a stacking method that intrinsically includes intragroup H I (see H23).

¹³ https://heasarc.gsfc.nasa.gov/

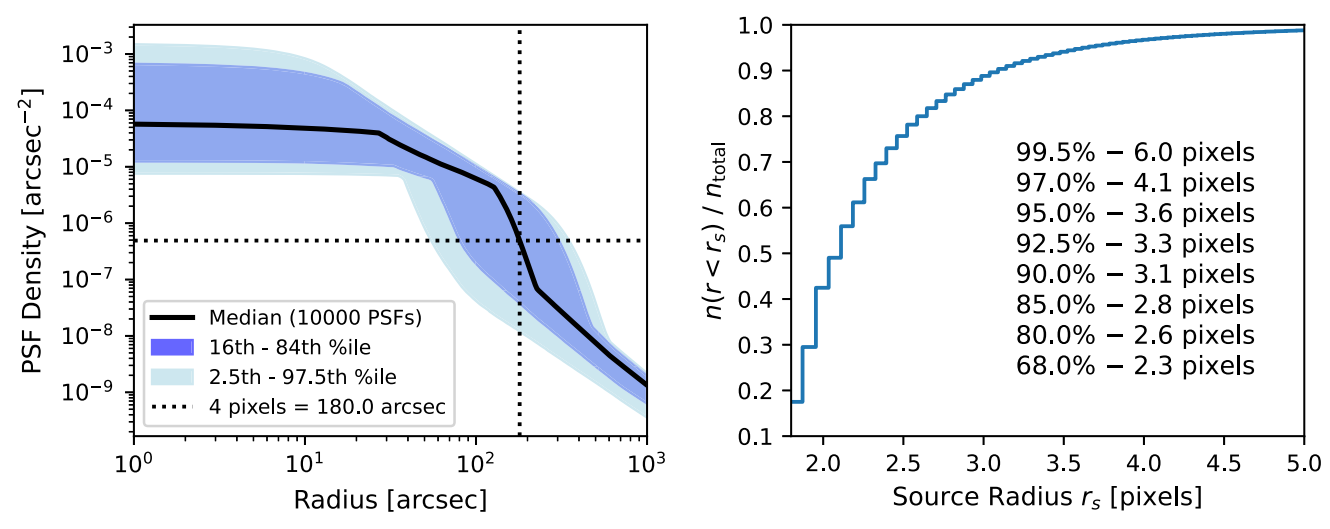


Figure 1. PSPC PSF and distribution of source radii. Left: distribution of 10,000 ROSAT PSPC PSFs calculated with random photon energies spanning 0.44–2.04 keV and random off-axis angles spanning 0'–60'. The solid black line shows the median PSF; blue shaded regions show the 16th–84th (dark) and 2.5th–97.5th (light) percentiles of the distribution at fixed radius. Dotted lines show the PSF strength at a radius of 4 pixels (180"). Right: cumulative distribution function $n (r < r_s)/n_{\text{total}}$ describing the fraction of ROSAT sources, as identified with the iterative sigma-clipping algorithm described in Section 3.1, with radii less than r_s . Annotated values tabulate the percentage of sources with radii less than r_s .

do not want these galaxies to be automatically masked. We automatically masked the remaining 2RXS point sources (EXI_ML>9 and not cross-matched to RESOLVE/ECO) as described below.

To determine mask apertures for both RESOLVE/ECO AGN galaxies and 2RXS sources, we considered whether these sources could be matched to sources identified by our sigmaclipping algorithm. If so, we extracted masks from the segmentation map, which naturally provides a custom aperture for each source. If the RESOLVE/ECO AGN or 2RXS source was not detected by the sigma-clipping algorithm, we applied a circular mask with radius 4 pixels, where each RASS pixel is 45". As illustrated in Figure 1, this value was chosen because \sim 97% of the sources identified by the sigma-clipping algorithm can be enclosed by such an aperture. Figure 1 also shows that the median point-spread function (PSF) of the PSPC reaches \sim 1% of its maximum strength at this 4-pixel radius. We compute the median PSF from a sample of PSFs generated at random 0.44-2.04 keV photon energies and 0'-60' off-axis angles (the PSPC field of view), based on the analytic formula for the PSPC PSF (F. Boese 2000). This statistical PSF computation is necessary because RASS imaging data are coadds of multiple visits to each field; thus, sources in the RASS data have been observed at a variety of unknown offaxis angles.

In Section 4, to separate galactic and intragroup X-ray emission, we provide stacking results both with AGN masked and with AGN unmasked. In the former, we masked the locations of all RESOLVE and ECO AGN contained within the custom-mosaicked count maps. For both masked AGN and 2RXS sources, we replace masked regions with the background count level. Figure 2 illustrates an example of this masking procedure.

3.2. Scaling and Cropping Images

Since we wish to stack images of groups at different distances, it is crucial that we add RASS images on a consistent scale. Following X. Dai et al. (2007), we scaled our masked group images to a common kiloparsec-per-degree scale

matching the outer distance of the ECO survey ($100 \,\mathrm{Mpc}$ for our chosen Hubble constant $H_0 = 70 \,\mathrm{km \, s^{-1} \, Mpc^{-1}}$) to ensure that all pixel resampling combines rather than oversamples pixels. The original 512×512 masked mosaics are then contained within an inner square region of the scaled image, bordered by zeros. The scaled images conserve the number of photons in the original image, with a typical error of <1%. Conservation of photon number is appropriate, as this rescaling procedure is not meant to simulate artificial redshifting of groups. Rather, it enables us to stack individual group images on a common physical scale, i.e., to ensure that halos of the same mass are stacked consistently even if they are located at different distances. We also applied this same scaling procedure to our exposure and background count maps, which are needed to perform stacking.

Prior to stacking, we cropped our scaled count, exposure, and background maps to centered 219 × 219 pixel cutouts. At the RASS 45" pixel scale and our outer survey distance limit of 100 Mpc, the 219-pixel image width corresponds to 4.7 Mpc on sky. Importantly, cropping to 219 × 219 removes the zero-containing border regions left over from image scaling, even for the nearest ECO galaxy groups at ~42.9 Mpc (noting that 512 pixels × 42.9 Mpc/100 Mpc = 219 pixels), but still comfortably contains our largest groups with $R_{\rm vir} \sim 1.7$ Mpc. The last panel of Figure 2 shows an example of a scaled and cropped count map.

3.3. Image Stacking and Signal-to-noise Ratio Calculation

In Section 4, we present X-ray stacking results binned by halo mass and other group properties. To construct the stacked images, we applied stacking methods from prior RASS analyses (X. Dai et al. 2007; M. E. Anderson et al. 2012, 2015). For each stacking bin consisting of a set of n_{bin} groups, we have a set of masked count maps $\{C_1, C_2, ..., C_{n_{\text{bin}}}\}$, exposure maps $\{E_1, E_2, ..., E_{n_{\text{bin}}}\}$, and background maps $\{B_1, B_2, ..., B_{n_{\text{bin}}}\}$. We summed these sets to obtain a stacked count map $\mathcal{C} = \sum_{i=1}^{n_{\text{bin}}} C_i$ in counts, a stacked exposure map $\mathcal{E} = \sum_{i=1}^{n_{\text{bin}}} E_i$ in seconds, and a stacked background map $\mathcal{B} = \sum_{i=1}^{n_{\text{bin}}} B_i$ in

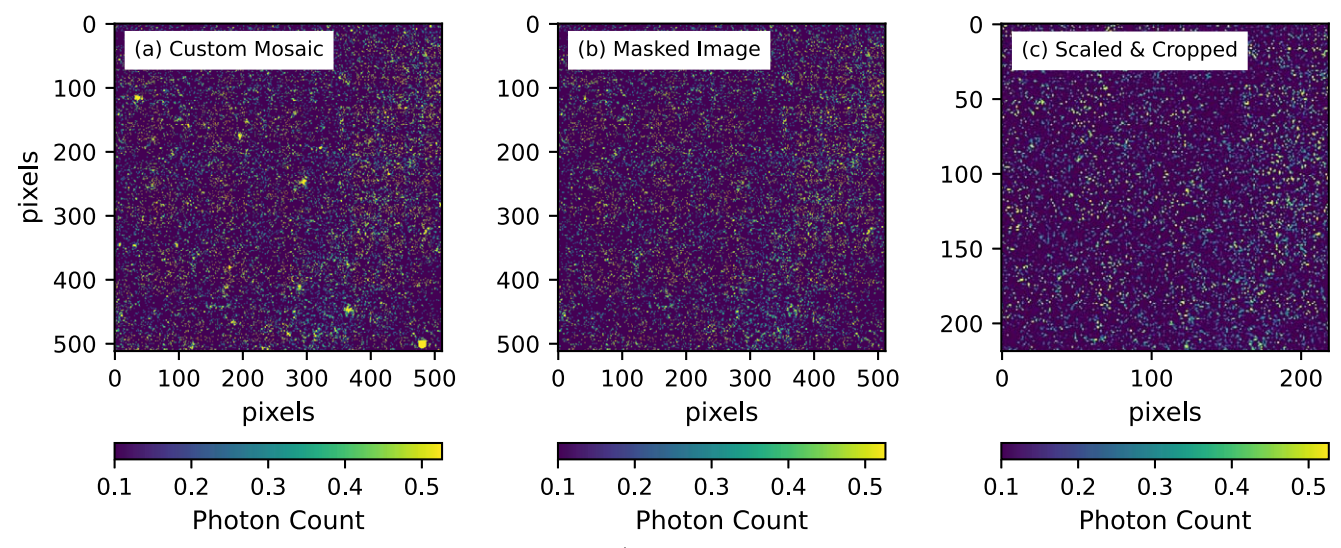


Figure 2. Demonstration of RASS image mosaicking, masking, and scaling/cropping applied to G3 group #93 (chosen arbitrarily for illustration). (a) Custom count map centered on group #93. Pixel values are in units of photon counts and may be fractional given that the original RASS data have been reprojected and mosaicked as described in Section 2.2. (b) Masked count map, with 2RXS point sources masked, as outlined in Section 3.1. (c) Scaled image cropped to a 219 × 219 pixel cutout, as detailed in Section 3.2.

counts. We compute the final background-subtracted intensity map for each stack as $\mathcal{R} = (\mathcal{C} - \mathcal{B})/\mathcal{E}$, in units of counts s⁻¹. ¹⁴

For each stack, we have accounted for source confusion by excluding pairs of groups whose angular separation is less than either of their individual virial radii (i.e., at least one of the groups resides within R_{vir} of the other in projection). However, since intragroup X-ray emission is typically concentrated to only $0.1R_{\text{vir}}$ – $0.5R_{\text{vir}}$ (J. S. Mulchaey 2000), and because lowmass groups are less likely to show bright X-ray emission, we made an exception if the two confused groups have drastically different mass (>1 dex) and are separated by more than $R_{\text{vir,min}} + (1/2)R_{\text{vir,max}}$, where $R_{\text{vir,min}}$ is the virial radius of the lower-mass group and $R_{vir,max}$ is the virial radius of the highermass group. In these cases, the lower-mass group is unlikely to contaminate the X-ray stack containing the higher-mass group, so we only excluded the lower-mass group. Based on this definition of confusion, we have flagged and excluded $\sim 21\%$ of our groups from stacking. The fraction of groups retained as a function of halo mass is approximately constant at \sim 70%–80%.

After constructing stacks and excluding confused objects, we computed the X-ray signal-to-noise ratio (SNR) within $0.5R_{\rm vir}$ for each stack, where $R_{\rm vir}$ is calculated using the halo mass at the bin center. The choice of $0.5R_{\rm vir}$ stems from the typical concentration of emission in X-ray-detected galaxy groups (J. S. Mulchaey 2000). Following S. De Grandi et al. (1997), we calculate the SNR as $N_{\rm src}/\sqrt{N_{\rm total}}$, where $N_{\rm src}$ and $N_{\rm total}$ are the numbers of source counts and total (background + source) counts, respectively, within the $0.5R_{\rm vir}$ aperture. We report an SNR of zero when the stacked background-subtracted count rate is zero or negative, which is possible because the RASS background maps are smooth whereas the RASS count maps are noisy. We also compute the total count rate within $0.5R_{\rm vir}$, as well as its uncertainty $\sigma_{\rm rms}/N$, where $\sigma_{\rm rms}$ is the rms noise

of the intensity map and N is the number of pixels in the $0.5R_{\rm vir}$ aperture.

3.4. Randomized Stacking

SNR alone is not sufficient to justify a claim that we have detected diffuse X-ray emission associated with G3 groups, as (compact or diffuse) foreground or background X-ray sources landing within the group virial radius could create a false signal. To quantify possible contributions from such sources, we replicated our data processing and stacking procedures using a set of images extracted at random sky positions. We generated 4093 (the total number of $N_{\rm galaxies} \geqslant 1$ groups with $M_{\rm halo} = 10^{11} - 10^{11.5} M_{\odot}$, our largest stacking bin) sets of count maps, exposure maps, and background count maps at R.A. and decl. sampled randomly from the RESOLVE and ECO footprints, avoiding sky positions within a projected $2R_{\rm vir}$ of any known groups. By extracting these images within the RESOLVE and ECO footprints, we have avoided Galactic X-ray emission at low Galactic latitudes and ensured that our random images have the same statistical properties as the G3 group images.

For each stacking bin containing $n_{\rm bin}$ G3 groups, we sampled the 4093 image sets with replacement to create 30 random image set samples. For each of the 30 samples, we masked, scaled, cropped, and stacked the random $n_{\rm bin}$ images so that they were processed identically to the image sets for the corresponding $n_{\rm bin}$ G3 groups assigned to that bin. The final product for each bin is a set of 30 stacks, which allows us to analyze the distributions of SNR and integrated count rate found in random image stacks.

3.5. Estimating X-Ray Binary Contributions

In Section 4, to help in understanding the origins of our stacked X-ray emission, we have provided for each stacking result the expected count rate from low-mass X-ray binaries (LMXBs) and high-mass X-ray binaries (HMXBs). To estimate these contributions, we considered multiple estimates of X-ray binary (XRB) scaling relations from the literature, including estimates for LMXB-only emission (L. P. David et al. 2006;

¹⁴ We note that averaging intensity maps directly, i.e., $\mathcal{R} = (1/n_{\text{bin}}) \sum (C_i - B_i)/E_i$, will yield the same result when E_i is the same for all groups. However, RASS coadd exposure times vary substantially across the sky (e.g., W. Voges et al. 1999, Figure 1), so we follow X. Dai et al. (2007) and M. E. Anderson et al. (2015) in using $\mathcal{R} = (\mathcal{C} - \mathcal{B})/\mathcal{E}$. This definition provides a more robust average, especially for our low- n_{bin} stacks.

B. Boroson et al. 2011; B. D. Lehmer et al. 2020), HMXB-only emission (S. Mineo et al. 2012, 2014; B. D. Lehmer et al. 2022), and total XRB emission (E. J. Colbert et al. 2004; B. Lehmer et al. 2010; B. D. Lehmer et al. 2019, 2024). Including all 3×3 possible pairs of these LMXB-only and HMXB-only estimators, we obtained 13 distinct estimators of total XRB emission. Next, for each stack, we computed exposure-weighted mean group-integrated properties (e.g., SFR, sSFR, L_K , M_*) as needed to evaluate these estimators and derive expected XRB luminosity estimates for the stack. Finally, we converted these luminosities to fluxes and converted the fluxes to expected RASS count rates using the Portable, Interactive, Multi-Mission Software (PIMMS; K. Mukai 1993). We used each paper's reported spectral model to convert to the PSPC hard band, correcting for foreground absorption using Galactic HI column densities from the gdpyc Python library, which are based on the Leiden/Argentine/Bonn Galactic H I Survey (P. M. Kalberla et al. 2005).

Using these 13 estimators, we report for each stack in Section 4 the minimum and maximum estimated XRB contributions and our preferred estimated XRB contribution. The XRB contribution increases with group halo mass for all estimators owing to the underlying increase of group $N_{\rm galaxies}$ with increasing halo mass. We have chosen the relation of B. D. Lehmer et al. (2019) as our default XRB estimator because (i) it is derived using a robust statistical sample of nearby galaxies with diverse morphologies, masses, and SF rates and (ii) it predicts RASS count rates consistent with our measured AGN-masked count rates within the uncertainties at low $M_{\rm halo}$, where X-ray emission should be dominated by XRBs. ¹⁵ Notwithstanding the good reasons for this choice of preferred estimator, we note that accurately estimating the contribution from XRBs is one of the greatest areas of uncertainty in this work and similar group X-ray stacking studies.

When analyzing X-ray stacks with AGN-host galaxies masked, we excluded these AGN-host galaxies' XRB contributions from our expected XRB count rate calculation, as any XRB emission from these galaxies will have been excluded by the AGN masks.

4. Results

4.1. How Do Cold Gas and Group X-Ray Emission Depend on Halo Mass?

Figure 3 shows stacked X-ray emission in six bins of group halo mass, chosen to coincide with regimes around the threshold and bimodality scales (see Section 1) and also to facilitate comparison with past work (e.g., M. E. Anderson et al. 2015). We provide total stacked count rates, stacked count rates with AGN galaxies masked, and expected XRB count rates. In all three cases, count rates increase as a function of halo mass.

With galaxies and AGN not masked ("all X-ray emission"), we detect X-ray emission with SNR > 2 in excess of the random stacks for all halo mass bins except $M_{\rm halo} = 10^{11} - 10^{11.5}\,M_{\odot}$, with more confident SNR > 4 detections at

 $M_{\rm halo}=10^{11.5}-10^{12.1}\,M_{\odot}$ and in the three individual bins spanning $M_{\rm halo}=10^{12.6}-10^{14.5}\,M_{\odot}$. Interestingly, the $M_{\rm halo}=10^{12.1}-10^{12.6}\,M_{\odot}$ bin shows a marginal 2.4σ detection despite being surrounded by more significant detections in adjacent bins. We speculate that this result may represent the confluence of decreasing $n_{\rm bin}$ (resulting in lower stacking depth) and increasing intrinsic X-ray emission as halo mass increases.

After AGN are masked, all count rates decrease relative to total count rates, although total and AGN-masked count rates are similar when considering their uncertainties. With AGN masked, we detect X-ray emission in excess of random stacking expectations in the three bins spanning $M_{\rm halo} = 10^{12.6} - 10^{14.5} M_{\odot}$, with the middle bin at $10^{13.3} - 10^{14} M_{\odot}$ reaching only a marginal SNR of 2.7 and the flanking bins reaching SNRs of 3.5 and 5.4.

Since masking AGN removes any AGN X-ray emission, ¹⁷ any remaining X-ray emission would be most likely attributed to XRBs or hot gas; thus, we compare to the expected XRB contribution for each stack. In the highest mass bin at $M_{\rm halo}=10^{14}-10^{14.5}\,M_{\odot}$, our preferred XRB estimate accounts for only $6\%\pm1\%$ of the observed AGN-masked count rate. In the next lower bins at $M_{\rm halo}=10^{13.3}-10^{14}\,M_{\odot}$ and $M_{\rm halo}=10^{12.6}-10^{13.3}\,M_{\odot}$, our preferred XRB estimates account for only $24\%\pm5\%$ and $33\%\pm4\%$, respectively, of the observed AGN-masked count rates. However, for these bins, our measured AGN-masked count rates are smaller than the highest estimates from the 13 XRB estimators we reviewed. Consequently, our results unambiguously confirm the presence of hot gas only for $M_{\rm halo}>10^{14}\,M_{\odot}$, though we consider our hot gas detections in the two bins spanning $M_{\rm halo}=10^{12.6}-10^{14}\,M_{\odot}$ to be reasonably secure. In lower halo mass bins, our observed AGN-masked count rates are consistent with or smaller than expectations for XRBs.

For comparison with the X-ray count rates, the bottom right panel of Figure 3 shows the distribution of $M_{\rm HI,grp}/M_{\rm halo}$ as a function of halo mass. From the lowest to highest halo mass bin, the median $M_{\rm HI,grp}/M_{\rm halo}$ drops by 1.1 dex (a factor of \sim 13) as the stacked X-ray intensity increases.

To highlight X-ray contributions driven by the group environment, Figure 4 assesses stacked X-ray emission excluding $N_{\rm galaxies}=1$ groups and considering only galaxy groups with halo masses $M_{\rm halo}=10^{11.5}-10^{14.5}\,M_{\odot}$, below which there are insufficient $N_{\rm galaxies}=1$ halos for stacking. With AGN not masked, Figure 4 shows X-ray emission in excess of random stacking expectations with SNR > 4 in the three bins spanning $M_{\rm halo}=10^{12.6}-10^{14.5}\,M_{\odot}$.

After masking AGN, the detections in these bins are maintained with lower SNR, although the $10^{13.3}-10^{14}\,M_\odot$ bin detection is still marginal as above. As in our Figure 3 analysis, comparing AGN-masked count rates and XRB expectations in Figure 4 shows that (i) only the $M_{\rm halo}=10^{14}-10^{14.5}\,M_\odot$ bin has an AGN-masked count rate that exceeds all 13 XRB estimators we considered, with our preferred XRB estimator accounting for just $6\%\pm1\%$ of the observed AGN-masked count rate, and (ii) our preferred XRB estimator accounts for just $24\%\pm5\%$

¹⁵ We prefer the relation of B. D. Lehmer et al. (2019) to that of B. D. Lehmer et al. (2024) because the latter yields XRB estimates that are systematically higher than our measured count rates in bins where the emission should be dominated by XRBs. The estimates from B. D. Lehmer et al. (2024) exceed our AGN-masked count rates in the three halo mass bins spanning $M_{\rm halo} = 10^{11} - 10^{12.6} \, M_{\odot}$, and they also exceed our total count rates (with AGN still included) in the $M_{\rm halo} = 10^{11} - 10^{11.5} \, M_{\odot}$ and $M_{\rm halo} = 10^{12.1} - 10^{12.6} \, M_{\odot}$ bins (see Section 4).

 $[\]overline{^{16}}$ The detection in the $M_{\rm halo}=10^{12.6}-10^{13.3}~M_{\odot}$ bin drops to SNR ~ 5.5 if we exclude group #1345, which contains an extremely X-ray-bright galaxy (ECO 04631/2RXS J141759.5+250817).

 $^{^{17}}$ Masking AGN may also mask intragroup hot gas in the foreground or background of the AGN-host galaxies, so our AGN-masked count rates are subject to this caveat. However, in each halo mass bin, the ratio of AGN-masked pixels to total stacked pixels is only $\sim 10\%$.

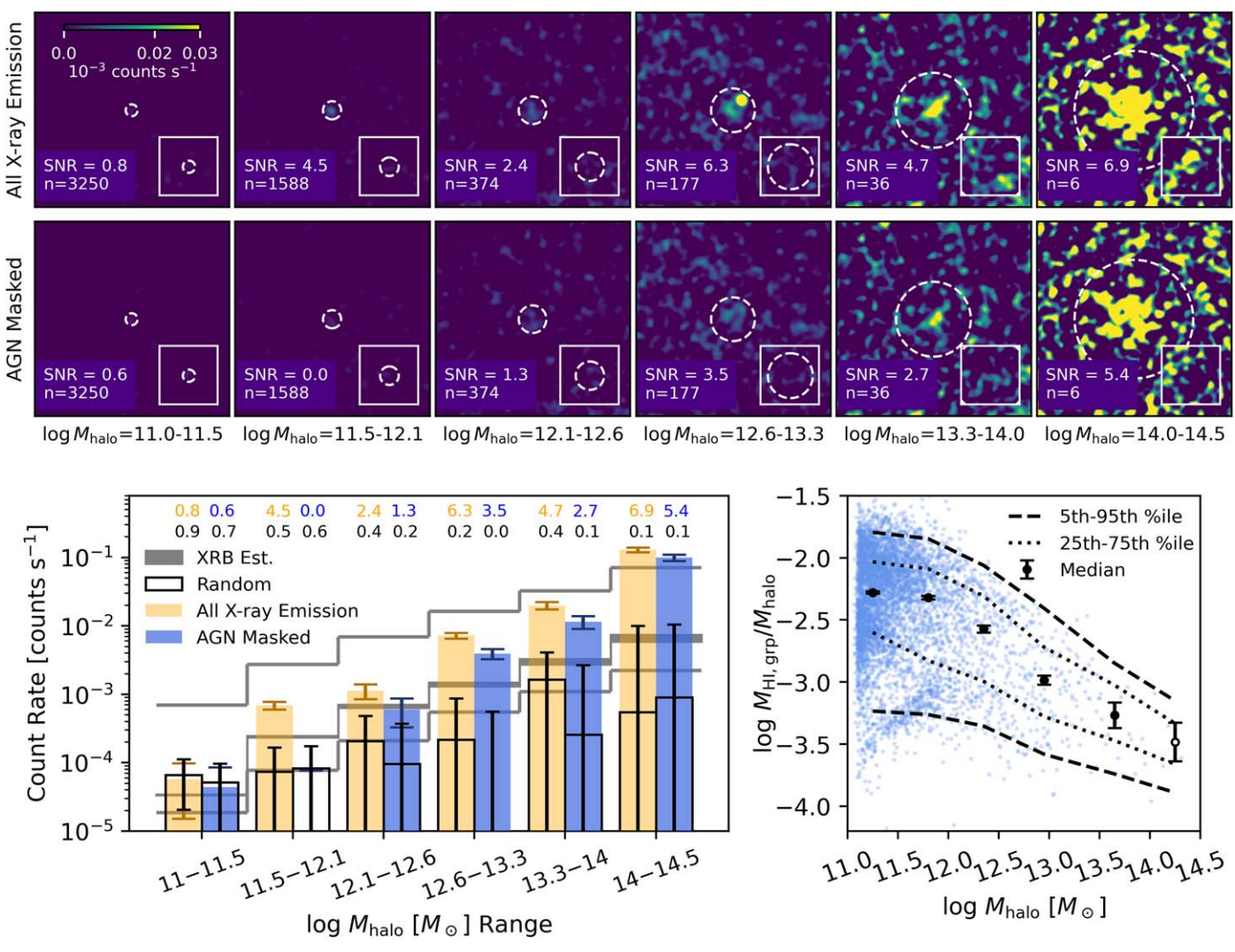


Figure 3. Stacked X-ray emission and group $M_{\rm HI,grp}/M_{\rm halo}$ in bins of group halo mass. $N_{\rm galaxies}=1$ groups are included. Top: stacked X-ray intensity maps when AGN galaxies are not masked. Images are smoothed with a 3-pixel Gaussian kernel to enable visualization on a common linear scale, as logarithmic scales emphasize noise fluctuations in low- $n_{\rm bin}$ stacks. White circles represent $R_{\rm vir}$ for a group at the center of the halo mass bin, with values of 0.14, 0.22, 0.33, 0.54, 0.91, and 1.45 Mpc from left to right. The annotations note the SNR and $n_{\rm bin}$ for each stack. Middle: same as the top row, but now with AGN masked. Bottom left: stacked, background-subtracted X-ray count rate as a function of halo mass for all intensity maps shown. Orange bars represent total count rates (AGN not masked); blue bars represent count rates with AGN masked. Black bars show the median count rate based on random stacking, and gray lines show estimates for XRB contributions. The top and bottom thin gray lines show the maximum and minimum estimates from the 13 different XRB estimators we considered (see Section 3.5). The middle thick gray line shows our preferred estimates using the B. D. Lehmer et al. (2019) calibration, where the width of the line indicates the uncertainty into seased on bootstrapping. The annotations list the SNR for each stack, with SNRs from randomized stacks in black. Bottom right: $M_{\rm HI,grp}/M_{\rm halo}$ vs. $M_{\rm halo}$ as in H23. Black points represent median values with errors determined using bootstrapping; open circles represent median values in bins with fewer than 30 groups, for which bootstrap errors may be unreliable. The dashed and dotted lines represent the 5th–95th and 25th–75th percentiles, respectively.

and $30\% \pm 4\%$, respectively, of the AGN-masked count rates in the two lower $M_{\rm halo} = 10^{13.3} - 10^{14} \, M_{\odot}$ and $M_{\rm halo} = 10^{12.6} - 10^{13.3} \, M_{\odot}$ bins, indicating likely hot gas detections in these bins as well. Although other XRB estimators among the 13 we considered could fully explain these bins' AGN-masked emission, the same estimators would overpredict the emission in lower mass bins.

The right panel of Figure 4 shows the corresponding distribution of $M_{\rm HI,grp}/M_{\rm halo}$ as a function of halo mass. Group H I content smoothly declines by 1.2 dex over the same halo mass range in which X-ray counts increase. Based on expected XRB contributions, our detections of diffuse X-rays from hot gas become confident across $M_{\rm halo} = 10^{12.6} - 10^{14} \, M_{\odot}$ and unambiguous above $M_{\rm halo} = 10^{14} \, M_{\odot}$, where $M_{\rm HI,grp}/M_{\rm halo}$ simultaneously reaches its lowest values as a function of halo mass. Together, these results suggest an inverse relationship

between halo-integrated H I content and halo-integrated X-ray emission, reflecting both hot gas and galactic X-ray sources. This relationship is discussed further in Section 5.

4.2. How Do Group Cold Gas and X-Ray Emission Depend on Virialization State at Fixed Halo Mass?

With their halo mass dependence established, we can now assess how group H I content and X-ray emission depend on virialization state, as parameterized by crossing time, at fixed halo mass. Figure 5 shows groups distributed in $M_{\rm HI,grp}/M_{\rm halo}$ versus $t_{\rm cross}$, in three panels representing bins of group halo mass. Analysis of $t_{\rm cross}$ requires $N_{\rm galaxies} > 1$ groups, so we again exclude $M_{\rm halo} < 10^{11.5} M_{\odot}$. For $M_{\rm halo} = 10^{11.5} - 10^{12.1} M_{\odot}$ and $M_{\rm halo} = 10^{12.1} - 10^{12.6} M_{\odot}$, Figure 5 shows a transition to greater spread in $M_{\rm HI,grp}/M_{\rm halo}$ as crossing time

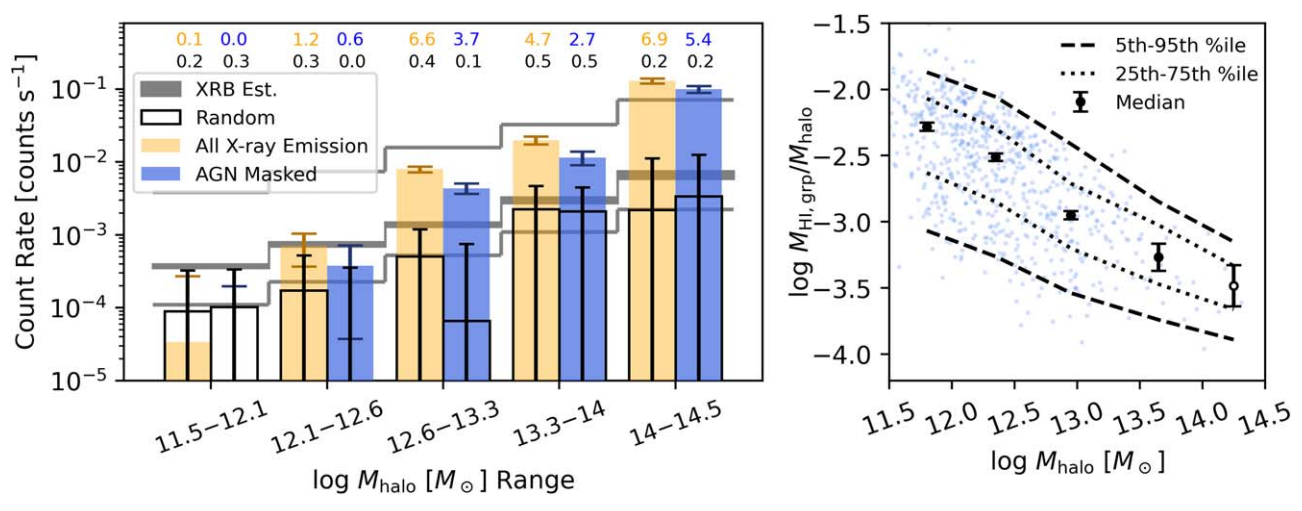


Figure 4. Group stacked X-ray emission and $M_{\rm HI,grp}/M_{\rm halo}$ in bins of group halo mass, as presented in the bottom row of Figure 3, but now excluding groups with $N_{\rm galaxies} = 1$ and/or $M_{\rm halo} < 10^{11.5} \, M_{\odot}$. The annotated numbers in the right panel give $n_{\rm bin}$ values for each bin, which are the same for both left and right panels. In the right panel, errors on the data points come from bootstrapping, and open circles represent bins with fewer than 30 groups, for which bootstrap errors may be unreliable.

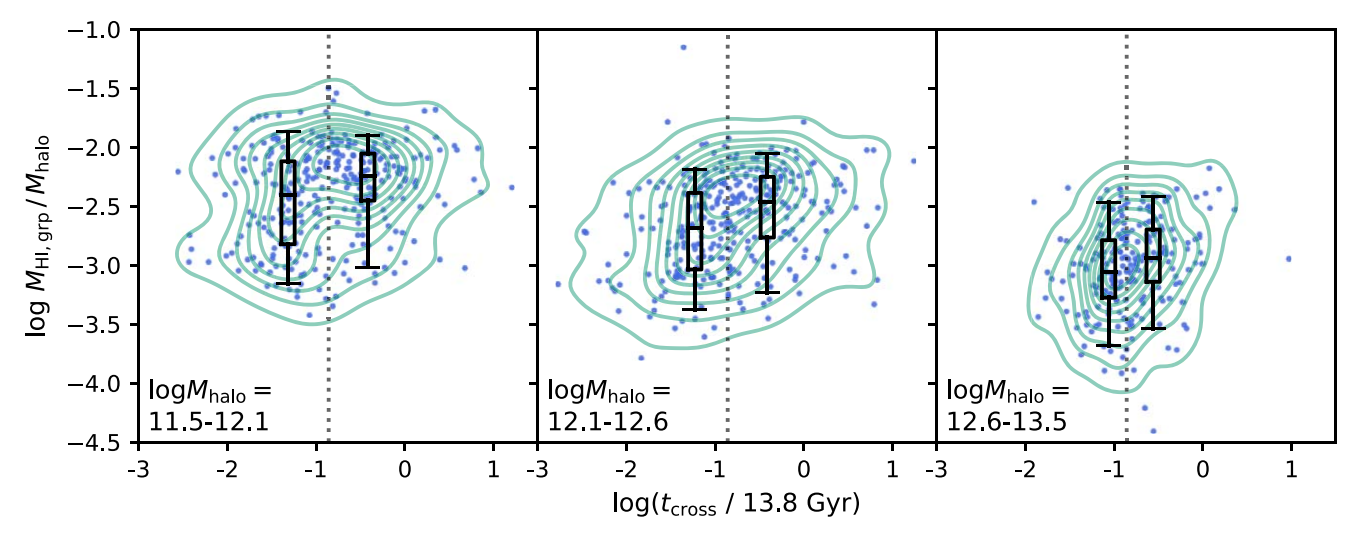


Figure 5. Group-integrated H I-to-halo mass ratios $(M_{\rm HI,grp}/M_{\rm halo})$ as a function of group crossing time, expressed as a fraction of the age of the Universe, in three halo mass bins. Contour lines have been drawn using kernel density estimation. The vertical line corresponds to $\log(t_{\rm cross}/13.8~{\rm Gyr}) = -0.86~(\sim 2~{\rm Gyr})$, as used in Section 4.2 to categorize groups as lower $t_{\rm cross}$ or higher $t_{\rm cross}$. Box plots show the distributions of $M_{\rm HI,grp}/M_{\rm halo}$ above and below $\log(t_{\rm cross}/13.8~{\rm Gyr}) = -0.86$ in each panel. The solid bar represents the median value, the box represents the interquartile range, and the whiskers show the 5th–95th percentiles. At crossing times smaller than $\log(t_{\rm cross}/13.8~{\rm Gyr}) = -0.86$, groups show greater diversity in H I content (particularly at lower $M_{\rm halo}$), as discussed in Section 4.2.

decreases, with many more low $M_{\rm HI,grp}/M_{\rm halo}$ values appearing despite the upper end of the range not changing. We see this transition occurring across $\log [t_{\rm cross}/13.8~{\rm Gyr}] \sim -0.86$ (marked with a vertical line), which is similar to the median values of $\log [t_{\rm cross}/13.8~{\rm Gyr}]$ in the bins shown (-0.89, -0.85, and -0.86, respectively) and represents $\sim 2~{\rm Gyr}$. The existence of this transition motivates us to ask whether X-ray emission increases below the same $t_{\rm cross}$ value, possibly due to virial shock heating and/or environmental triggering of SF or AGN.

To address this question, we provide two figures connecting group H I content (Figure 6) and X-ray emission (Figure 7) to $t_{\rm cross}$. In Figure 6, we show trends of median $M_{\rm HI,grp}/M_{\rm halo}$ versus $M_{\rm halo}$ for lower- $t_{\rm cross}$ and higher- $t_{\rm cross}$ groups, which are separated at $\log(t_{\rm cross}/13.8~{\rm Gyr}) = -0.86$ based on Figure 5. Lower- $t_{\rm cross}$ groups exhibit lower median $M_{\rm HI,grp}/M_{\rm halo}$ than

higher- t_{cross} groups at fixed halo mass, with a maximum difference of 0.2 dex (a factor of \sim 1.6). We note that while Figure 6 includes X-ray confused groups in calculations (whereas Figure 7 excludes these groups), the trends in Figure 6 are not noticeably different if these confused groups are excluded.

Figure 7 illustrates stacked X-ray count rates for galaxy pairs and groups in the same $M_{\rm halo}$ bins and $t_{\rm cross}$ categories as in Figure 6. With AGN not masked, as shown in the left panel, we find SNR > 4.5 detections for both $t_{\rm cross}$ categories at $M_{\rm halo} = 10^{12.6} - 10^{13.3} \, M_{\odot}$. In the $M_{\rm halo} = 10^{13.3} - 10^{14} \, M_{\odot}$ and $M_{\rm halo} = 10^{14} - 10^{14.5} \, M_{\odot}$ bins, we find weak SNR ~ 2.8 detections for higher- $t_{\rm cross}$ bins and significant SNR $\geqslant 4.9$ detections for lower- $t_{\rm cross}$ bins. The measured count rate exceeds random stacking expectations in all cases. We note that if we exclude group #1345 (see footnote 16) from the higher- $t_{\rm cross}M_{\rm halo} = 10^{12.6} - 10^{13.3} \, M_{\odot}$ bin, the SNR of that stack drops to 4.

 $^{^{18}}$ For both Figures 6 and 7, our results do not noticeably change when adopting boundary values of -0.75 or -1 instead of our chosen value of -0.86.

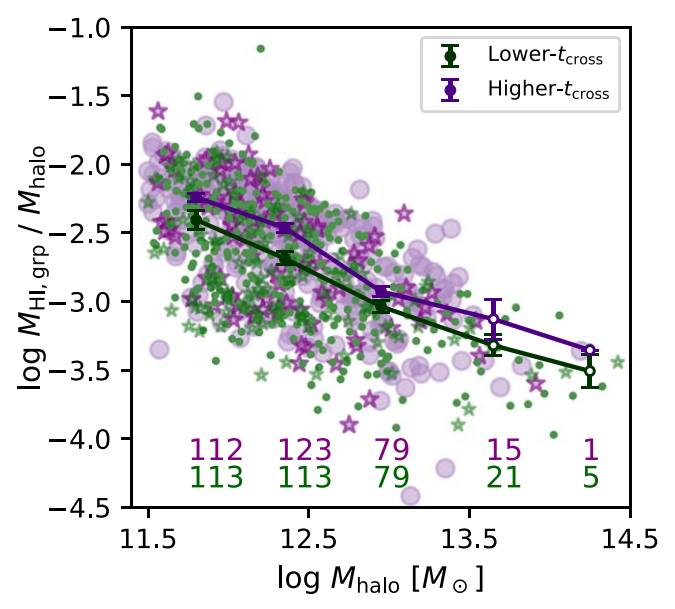


Figure 6. Median $M_{\rm HLgrp}/M_{\rm halo}$ vs. $M_{\rm halo}$ for lower- $t_{\rm cross}$ (green) and higher- $t_{\rm cross}$ (purple) groups, as defined in Section 4.2. We exclude $N_{\rm galaxies}=1$ groups from this plot. Error bars on the medians were computed using bootstrapping with 5000 resamples; open circles represent bins that contain too few (<30) groups to attain reliable bootstrapped errors. X-ray confused groups are marked with stars rather than points. The numbers of groups within each bin, excluding X-ray confused groups (to match Figure 7), are annotated at the bottom.

The SNRs of these detections drop when AGN are masked, as illustrated in the right panel, and in this case we still find SNR \geqslant 2.9 detections in excess of random stacks for higher- $t_{\rm cross}$ groups at $M_{\rm halo}=10^{12.6}-10^{13.3}\,M_{\odot}$ and for lower- $t_{\rm cross}$ groups in the two bins spanning $M_{\rm halo}=10^{13.3}-10^{14.5}$. There is additionally a weaker SNR \sim 2.2 detection for lower- $t_{\rm cross}$ groups at $M_{\rm halo}=10^{12.6}-10^{13.3}\,M_{\odot}$, consistent with XRB expectations. The most significant detection is for lower- $t_{\rm cross}$ groups at $M_{\rm halo}=10^{14}-10^{14.5}\,M_{\odot}$, where the SNR reaches 5.9.

With these results, we cannot confidently ascertain whether a general relationship exists between group X-ray emission and group crossing time at fixed halo mass. There is a hint, however, that enhanced group X-ray emission from hot gas or galactic sources is associated with greater virialization (lower $t_{\rm cross}$) above $M_{\rm halo} = 10^{13.3} M_{\odot}$. With AGN masked, the low- $t_{\rm cross}$ bins at $M_{\rm halo} = 10^{13.3} - 10^{14} M_{\odot}$ and $M_{\rm halo} = 10^{14} - 10^{14.5} M_{\odot}$ show enhanced count rates, of which (based on our preferred XRB estimator) XRBs are expected to contribute $22\% \pm 4\%$ and $4\% \pm 1\%$, respectively. This result flips in the lower $M_{\text{halo}} = 10^{12.6} - 10^{13.3} M_{\odot}$ halo mass bin, where higher- t_{cross} groups show enhanced count rate. In this case, XRBs contribute $15\% \pm 3\%$. Deeper X-ray data over a larger number of groups would be needed to confirm and better understand these results. The binning of our sample by both M_{halo} and t_{cross} , on top of excluding $N_{\text{galaxies}} = 1$ halos and confused halos, leaves us <125 groups per stacking bin, thereby reducing our stacking depth and increasing our sensitivity to outliers. We further discuss these results and their connection to group H I content in Section 5.2.

4.3. How Do Group Cold Gas Content and X-Ray Emission Depend on AGN and Star Formation at Fixed Halo Mass?

Figures 8–10 assess how AGN and SF relate to cold gas content and X-ray emission. Figure 8 shows trends of median

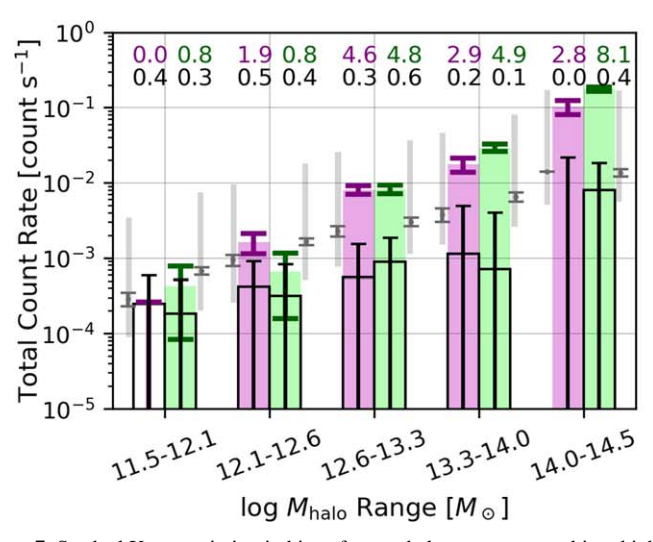
 $M_{\rm HI,grp}/M_{\rm halo}$ and FSMGR_{grp}, dividing our sample into AGN-hosting and non-AGN-hosting halos. $N_{\rm galaxies}=1$ halos are included. Trend lines are computed in sliding 0.3 dex halo mass bins. The sliding statistic helps us better identify fine structure in the data that might be suppressed by discrete binning. However, we also superpose points with error bars (derived from bootstrapping) for independent 0.3 dex bins.

Figure 8 demonstrates that below the bimodality scale of $M_{\rm halo} = 10^{12.1} \, M_{\odot}$ halos with AGN have reduced median $M_{\rm HI}$ $_{\rm grp}/M_{\rm halo}$ and FSMGR $_{\rm grp}$ compared to halos without AGN. The reduced $M_{\rm HI,grp}/M_{\rm halo}$ for AGN-hosting halos is significant to $>5\sigma$ according to a two-sample Kolmogorov–Smirnov test, and it reaches a depth of ~ 0.4 dex at $\log M_{\rm halo} = 11.5 \pm 0.1$. Within this halo mass range, non-AGN-hosting halos exhibit a plateau in $M_{\rm HI,grp}/M_{\rm halo}$, whereas AGN-hosting halos exhibit a broad valley in $M_{\rm HI,grp}/M_{\rm halo}$ over 1 dex in halo mass centered on $\log M_{\rm halo} = 11.8 \pm 0.1$ (based on a parabolic fit to the valley labeled "a" in Figure 11). Valley "a" underlies the noticeable yet narrower depression in $M_{\rm HI,grp}/M_{\rm halo}$ ratios labeled "b" that is seen for all halos (black line), which occurs across $M_{\rm halo} \sim 10^{11.6} - 10^{12} \, M_{\odot}$ as the fraction of halos with AGN rises, crossing 50% at $\log M_{\rm halo} \sim 10^{11.7} M_{\odot}$. To assess the statistical significance of valley "b," we constructed a baseline for our median $M_{\rm HI,grp}/M_{\rm halo}$ versus $M_{\rm halo}$ data by fitting to the analytic model of A. Obuljen et al. (2019), resulting in $\log M_0 = 9.4$, $\log M_{\min} = 11.3$, and $\alpha = 0.39$ (see also H23), and then divided the integrated area above the valley into the integrated noise expected from our uncertainties in the median values. This calculation indicates a confidence of 3.5σ for valley "b" across $M_{\rm halo} = 10^{11.6} - 10^{12.1} \, M_{\odot}$. While we lack a model baseline to quantify the larger valley "a" seen for AGN-hosting halos taken alone, the fact that it represents a $>5\sigma$ deviation from non-AGN-hosting halos provides a physical explanation for valley "b" and compels us to consider both valleys meaningful.

Above the bimodality scale, we note another potential valley in the trend for AGN-hosting halos located at approximately $M_{\rm halo}\sim 10^{12.7}-10^{13.3}\,M_{\odot}$ (labeled "c" in Figure 11), which is mirrored in the trend for all halos. This high-mass valley deviates from our model fit to the median $M_{\rm HI,grp}/M_{\rm halo}$ versus $M_{\rm halo}$ relation (see above) with a significance of 3.9 σ ; however, this deviation could also be interpreted as a 1.3σ bump at $\log M_{\rm halo} \sim 13.3$ rather than a valley at $\log M_{\rm halo} \sim 13.0$. If the high-mass valley labeled "c" in Figure 11 is truly a valley rather than a positive bump, it has higher significance than the narrow valley labeled "b," which has a demonstrable physical origin in the (larger and more significant) valley labeled "a." Finally, given concerns about the reliability of mid-IR AGN classifications in the dwarf regime (e.g., K. N. Hainline et al. 2016; M. R. Sturm et al. 2025), we note that our results in Figure 8 do not noticeably change if we treat mid-IR AGN-host galaxies as non-AGN-hosting galaxies, due to their relative infrequency (2.5% of our AGN).

To investigate whether these relationships may have associated X-ray emission signatures reflecting galactic X-ray

¹⁹ Given that our calculated FSMGRs (see Section 2.1.3) could reflect potential systematics associated with SED fitting (S. Lower et al. 2020), we have confirmed that our result still holds if we instead calculate FSMGR_{grp} using UV and mid-IR photometry from M. S. Polimera et al. (2025, in preparation). These alternative FSMGRs have been calculated using standard composite SFR prescriptions (V. Buat et al. 2011), which typically assume a constant SF history over a relatively short timescale ∼100 Myr, and they rely on SED fitting only in the use of internal extinction corrections.



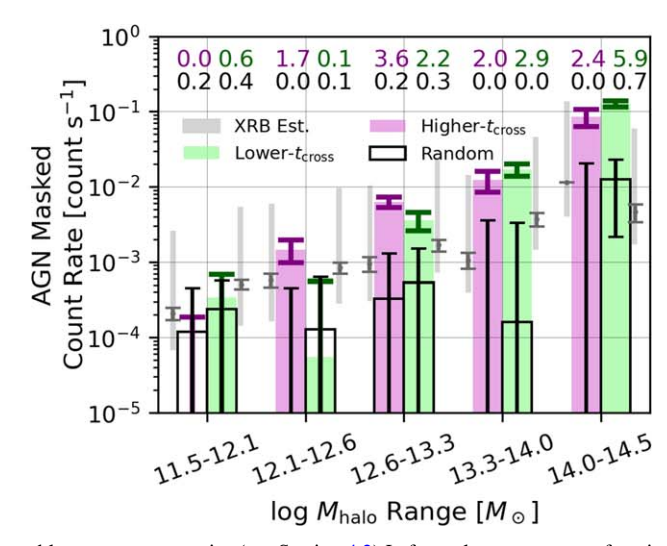


Figure 7. Stacked X-ray emission in bins of group halo mass separated into higher- and lower- t_{cross} categories (see Section 4.2) Left: total count rate as a function of halo mass for lower- t_{cross} (green) and higher- t_{cross} (pink) groups. Black lines represent count rates for random stacks. Gray points and error bars represent our preferred XRB estimate and its uncertainty from bootstrapping, while the gray bars represent the range between the minimum and maximum XRB estimator for each stack. Numbers annotated at the top are SNRs for each stacking bin, with SNRs corresponding to random stacking in black. Right: same as the left panel, but count rates are measured with AGN masked.

sources or hot gas, Figure 9 shows background-subtracted X-ray count rates versus halo mass for AGN-hosting and non-AGN-hosting halos, measured with AGN unmasked. We have stacked halos in bins up to $M_{\rm halo}=10^{12.1}-10^{12.6}\,M_{\odot}$, the highest mass bin that contains non-AGN-hosting halos. For non-AGN-hosting halos, we do not detect significant X-ray emission in any of the bins. However, for AGN-hosting halos, we detect SNR > 3 X-ray emission in excess of random stacking expectations in the two halo mass bins spanning $M_{\rm halo}=10^{11.5}-10^{12.6}\,M_{\odot}$ but not from the lower mass bin at $M_{\rm halo}=10^{11}-10^{11.5}\,M_{\odot}$. To test whether the excess emission arises from or near the AGN, we replicated the analysis of Figure 9 but instead masked known AGN (not pictured). The detections in the $M_{\rm halo}=10^{11.5}-10^{12.6}\,M_{\odot}$ and $M_{\rm halo}=10^{12.1}-10^{12.6}\,M_{\odot}$ bins dropped to SNR < 2. This result confirms that some of the excess X-rays we measure in Figure 9 derive from AGN directly or from hot gas (possibly heated by AGN).

4.4. Connecting Crossing Time and AGN Results

Finally, we consider whether our separate results connecting group H I content to crossing time and to AGN/SF are related, as might occur if group assembly lowers $t_{\rm cross}$ and thereby increases the likelihood of triggering AGN or enhancing SF. This analysis requires that we exclude $N_{\rm galaxies}=1$ groups to calculate $t_{\rm cross}$, leaving only 410 AGN-hosting groups and only 30 non-AGN-hosting groups at all halo masses. Given this small number of non-AGN-hosting groups, as well as our inconclusive X-ray stacking results in Section 4.2 when binning in $M_{\rm halo}$ and $t_{\rm cross}$, we do not consider X-ray emission in this joint analysis.

Figure 10 shows the $M_{\rm HI,grp}/M_{\rm halo}$ versus $M_{\rm halo}$ relation subdivided into four bins, representing AGN-hosting and non-AGN-hosting halos, as well as lower- $t_{\rm cross}$ and higher- $t_{\rm cross}$ groups. Lines represent median values in sliding windows, and points represent medians and errors in independent 0.4 dex bins on the sliding median trend line; as in Figure 8, the points may not overlap since for different subsamples the sliding medians start and end at different halo masses.

The left panel illustrates that AGN-hosting halos at higher $t_{\rm cross}$ have elevated $M_{\rm HI,grp}/M_{\rm halo}$ compared to AGN-hosting halos at lower $t_{\rm cross}$. At $M_{\rm halo} \sim 10^{12.5}-10^{13}\,M_{\odot}$ and higher masses, the median trend lines for higher- and lower- $t_{\rm cross}$ AGN-hosting halos become consistent, given the error bars and high- $t_{\rm cross}$ non-AGN-hosting halos have similar $M_{\rm HI,grp}/M_{\rm halo}$, albeit with the caveat that the bootstrapped uncertainties on $M_{\rm HI,grp}/M_{\rm halo}$ may not be reliable given the small number of $N_{\rm galaxies} > 1$ groups that lack AGN. Thus, a larger sample of non-AGN-hosting halos would be helpful for ascertaining whether the relationships connecting group H I content to group crossing time and AGN presence are independent.

5. Discussion

Our results in the previous section connect the relationship between group HI content and X-ray emission to group crossing time, SF, and AGN activity. We now discuss broader implications and compare to past observational and theoretical work. We first discuss the gas inventory in halos and then discuss possible physical scenarios relating virialization state, AGN, and SF to halo HI content.

5.1. The Gas Inventory in Halos

In Section 4.1, our results implied an inverse relationship between group H I content and the presence of hot intragroup gas. At high halo masses $M_{\rm halo} \gtrsim 10^{12.6}\,M_{\odot}$, groups have low H I-to-halo mass ratios, and their stacked X-ray count rates are unlikely to be fully explained by XRBs and AGN, ²⁰ suggesting

²⁰ Dwarf AGN appear to be typically underluminous in X-rays (L. J. Latimer et al. 2019; M. S. Polimera et al. 2025, in preparation). Moreover, among dwarf AGN detected using all the aforementioned methods, the "SF-AGN" identified by M. S. Polimera et al. (2022) are the most abundant and have the most dwarf-like host galaxy properties, i.e., metal-poor, gas-rich, and star-forming. The abundance of these "typical dwarf" AGN exceeds that of X-ray-detected dwarf AGN by at least a factor of five (comparing M. S. Polimera et al. 2022 to K. L. Birchall et al. 2022), so we do not expect an additional undetected dwarf AGN population with significant X-ray emission to contribute to our stacks, although we cannot rule it out.

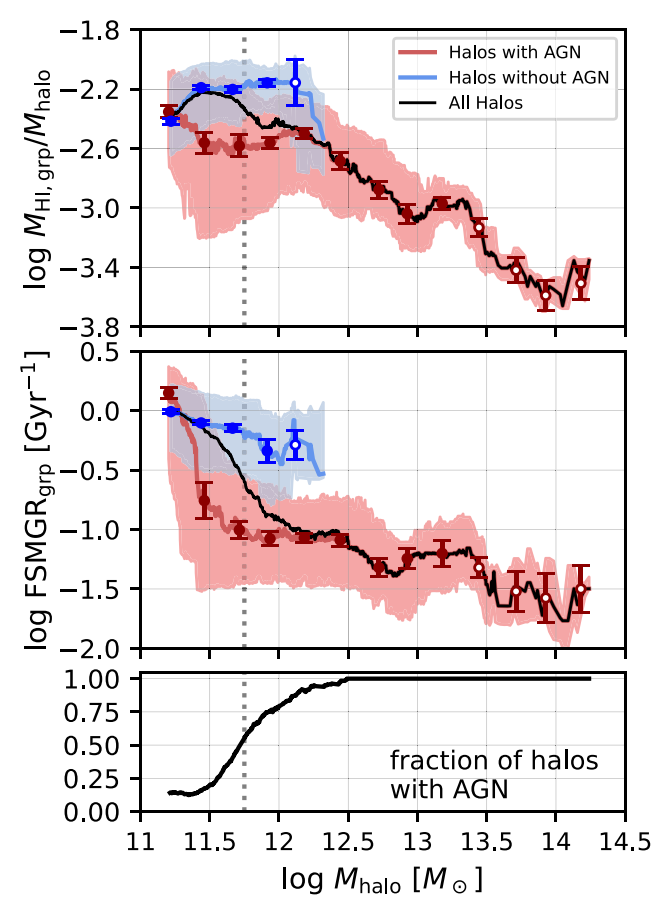


Figure 8. Median $M_{\rm HI,grp}/M_{\rm halo}$, median FSMGR_{grp}, and fraction of halos with AGN as a function of halo mass. All panels include $N_{\rm galaxies}=1$ groups. Top: median $M_{\rm HI,grp}/M_{\rm halo}$ vs. $M_{\rm halo}$ for halos with AGN (red) and without AGN (blue). Lines were generated using a sliding window, which advances forward in one-data-point increments to compute the median $M_{\rm HI,grp}/M_{\rm halo}$ and median $M_{\rm halo}$ values in overlapping 0.3 dex bins of halo mass. Data points show medians in independent 0.3 dex bins extracted from these sliding median trend lines, with error bars determined by bootstrapping; open data points denote bins for which the bootstrapped error is unreliable as a result of having <30 data points in the bin. As a consequence of the different sampling of AGN-hosting and non-AGN-hosting halos as a function of halo mass, the data points for the AGN-hosting and non-AGN-hosting selections do not fall at exactly the same halo mass values. Shaded regions represent the interquartile (middle 50%) range, also computed in a sliding window. Middle: median group-integrated FSMGR vs. M_{halo} for halos with and without AGN. Lines, colors, points, and shaded regions are as in the top panel. We note that the elevation of the lowestmass FSMGR_{grp} point for AGN-hosting halos is a binning artifact and not a robust result. Bottom: fraction of AGN-containing halos as a function of $M_{\rm halo}$, computed using a sliding 0.3 dex window in group halo mass.

the presence of diffuse hot gas. We found that lower-mass halos have higher H I-to-halo mass ratios and stacked X-ray emission that can probably be explained in full by AGN or XRBs.

X-ray detections at these high halo masses are expected from previous work. In a stacking analysis using RASS data, M. E. Anderson et al. (2012) detected strong X-ray emission from both early- and late-type luminous, isolated galaxies but reported that faint, isolated galaxies (central galaxy $K_s \geqslant -24.1$, typically $M_{\rm halo} \sim 10^{12.3}\,M_{\odot}$ in ECO) showed no evidence of extended emission. In a larger RASS stacking analysis of $\sim\!250,000$ SDSS BCGs, M. E. Anderson et al. (2015) further detected extended hot gas down to central galaxy $M_* = 10^{10.8}\,M_{\odot}$, corresponding to $M_{\rm halo} = 10^{12.6}\,M_{\odot}$. Furthermore, deeper X-ray observations using Chandra, XMM-

Newton, and eROSITA have measured hot gas luminosity versus group halo mass down to $M_{\rm halo} \sim 10^{11}\,M_{\odot}$ (D.-W. Kim & G. Fabbiano 2013; A. D. Goulding et al. 2016; D. A. Forbes et al. 2017; Á. Bogdán & M. Vogelsberger 2022; Y. Zhang et al. 2024). The steep slope of this power law highlights the much weaker X-ray emission of lower-mass halos in comparison to higher-mass halos. As such, our stacking analysis, despite being based on volume-limited, dwarf-dominated surveys, may have lacked enough low-mass halos (compared to these other studies) to detect hot gas at these low halo masses.

Scarcity of hot gas in low-mass halos would be consistent with both theoretical and observational expectations that most halo gas in these halos is in the form of the warm-hot intergalactic medium (WHIM). In simulations, WHIM constitutes 40%-50% of the baryonic mass inventory at temperatures and densities that emit only weakly in X-rays (R. Cen & J. P. Ostriker 1999; R. Davé et al. 2001; B. D. Smith et al. 2011). Examining the cold baryonic mass (stars + atomic gas) function in RESOLVE and ECO and combining it with literature prescriptions for hot halo gas and galactic molecular gas, K. D. Eckert et al. (2017) found a mass deficit below $M_{\rm halo} = 10^{12.1} \, M_{\odot}$ between the observed baryonic mass function and the expected baryonic mass function, based on the halo mass function and assuming a uniform baryonic fraction. This deficit matched theoretical estimates for WHIM in lowmass halos.

5.2. Group Virialization State

In Section 4.2, we demonstrated that lower- $t_{\rm cross}$ galaxy groups show statistically lower $M_{\rm HI,grp}/M_{\rm halo}$ ratios and greater spread in $M_{\rm HI,grp}/M_{\rm halo}$ than higher- $t_{\rm cross}$ groups at fixed halo mass. The transition to greater spread in group HI content occurs across $\log(t_{\rm cross}/13.8~{\rm Gyr}) = -0.86$, or $\sim 2~{\rm Gyr}$. It is interesting that this transition becomes prominent for $M_{\rm halo} = 10^{12.1} - 10^{12.6} M_{\odot}$ and even more so for $M_{\rm halo} = 10^{11.5} - 10^{12.1} M_{\odot}$, whereas at higher halo masses there is a smoother relationship between $M_{\rm HI,grp}/M_{\rm halo}$ and $t_{\rm cross}$ across this $\sim 2~{\rm Gyr}$ scale (see Figure 5).

Using a sample of 172 SDSS groups, M. Ai & M. Zhu (2018) have also examined the relationship between $M_{\rm HI,grp}$ $M_{\rm halo}$ and $t_{\rm cross}$. Their results do not appear to show such a transition to greater spread in $M_{\rm HI,grp}/M_{\rm halo}$ across $\log(t_{\rm cross}/13.8~{\rm Gyr}) = -0.86$, perhaps due to the higher halo masses of their groups, which span $M_{\rm halo} \sim 10^{13} - 10^{14.5}~M_{\odot}$. However, our results are consistent with theirs in showing suppressed median $M_{\rm HI,grp}/M_{\rm halo}$ for groups with lower $t_{\rm cross}$. Through comparison of crossing time to HI depletion timescales, the authors argued that this relationship implies that long-timescale processes (e.g., starvation; K. Bekki et al. 2002) are more important in group evolution than shorttimescale environmental quenching processes (e.g., ram pressure stripping; M. G. Abadi et al. 1999). These processes are usually associated with massive groups and clusters (due to their being more effective in environments with hot gas), but their effects have been seen in less massive halos around the bimodality scale and even below it (e.g., J. Grcevich & M. E. Putman 2009; T. Li et al. 2017; M. E. Putman et al. 2021; J. Zhu & M. E. Putman 2023; M. G. Jones et al. 2024). Thus, the continued trend we see down to $M_{\rm halo}=10^{11.5}-10^{12}\,M_{\odot}$ (Figure 6) is not surprising.

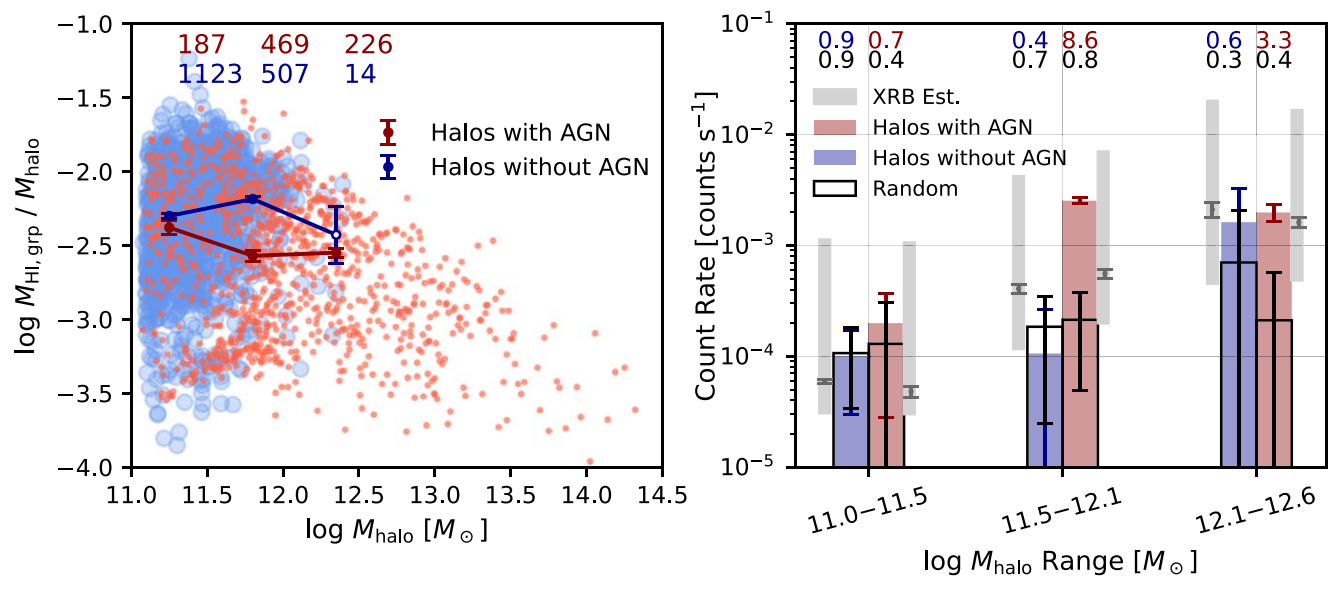


Figure 9. $M_{\rm HI,grp}/M_{\rm halo}$ and stacked X-ray emission for AGN-hosting and non-AGN-hosting halos in fixed halo mass bins. Left: median $M_{\rm HI,grp}/M_{\rm halo}$ vs. $M_{\rm halo}$ for AGN-hosting halos (red) and non-AGN-hosting halos (blue), following Figure 8 but now with halo mass bins matched to our X-ray stacks in the right panel. Open points denote bins for which the bootstrapped error bars are unreliable as a result of having <30 points. $N_{\rm galaxies} = 1$ halos are included. The numbers annotated at the top are the numbers of halos within each stacking bin, as used in the right panel. X-ray confused groups are excluded for consistency with the right panel. Right: stacked background-subtracted X-ray count rate vs. $M_{\rm halo}$ for AGN-hosting and non-AGN-hosting halos. Count rates are measured with RESOLVE and ECO AGN not masked. Annotated numbers are SNRs for the count rate measured in each stacking bin. Black points show our preferred XRB estimate based on B. D. Lehmer et al. (2019), and gray bars show the range of XRB estimates across all estimators (see Section 3.5).

In addition, mergers are expected to be common in halos typical of small groups, given the more effective dynamical friction at low peculiar velocities (S. Chandrasekhar 1943). Thus, the scatter toward low $M_{\rm HI,grp}/M_{\rm halo}$ in halos with low t_{cross} could alternatively reflect increased rates of H I processing in more compact halos. As groups collapse, mergers and interactions may become more frequent or more intense, and prior observations indicate that these interactions may trigger atomic gas consumption and associated feedback that may also deplete gas. Many studies have directly linked interactions and minor mergers to enhancement of AGN activity and SF (e.g., P. Di Matteo et al. 2008; D. V. Stark et al. 2013; S. Kaviraj 2014; A. Pipino et al. 2014; J. M. Comerford et al. 2015; F. Gao et al. 2020). It is possible, however, that the relationships connecting group H I to t_{cross} and AGN presence are independent; our result in Figure 10 includes too few non-AGN-hosting groups for us to say conclusively.

AGN aside, our X-ray emission results complicate the story. If lower $t_{\rm cross}$ truly indicates virialization state, AGN-masked X-ray count rates are greater for more-virialized groups at $M_{\rm halo} > 10^{13.3}\,M_{\odot}$ but greater for less-virialized groups at $M_{\rm halo} = 10^{12.6} - 10^{13.3}\,M_{\odot}$. These results follow expectations at high halo mass: above the "shutdown" scale at $\sim 10^{13.3}\,M_{\odot}$, models predict full halo gas heating to multiple virial radii (A. Dekel & Y. Birnboim 2006), and observations find that nearly all galaxies are gas-poor and quenched (S. J. Kannappan et al. 2009, 2013; A. J. Moffett et al. 2015).

et al. 2009, 2013; A. J. Moffett et al. 2015). The opposite result for $M_{\rm halo} = 10^{12.6} - 10^{13.3} \, M_{\odot}$ is an open puzzle. We note that crossing time is an imperfect metric of virialization state, and our broad categories of higher $t_{\rm cross}$ versus lower $t_{\rm cross}$ may oversimplify the full diversity of group H I content as a function of halo mass and virialization state. Groups with $M_{\rm halo} = 10^{12.6} - 10^{13.3} \, M_{\odot}$ are relatively small, so discrete merger events may make $t_{\rm cross}$ noisy. As group galaxies merge and the group evolves toward becoming a

"fossil group" (e.g., T. Ponman et al. 1994), the group H I content will drop (see H. Guo et al. 2020), but the group crossing time may not smoothly decrease. In fact, since galaxy mergers can remove some of the smallest group-relative on-sky distances from the $t_{\rm cross}$ calculation, crossing time could increase (contrary to expectations for increased virialization) after a merger. This scenario exemplifies that crossing time may not perfectly capture how H I content relates to group assembly, especially for small groups in which low velocity dispersions enable enhanced merging (e.g., R. Carlberg et al. 2001). Given this caveat and the additional complication that $t_{\rm cross}$ is subject to projection effects, future work on this topic may benefit from incorporating additional virialization metrics sensitive to merging history (e.g., magnitude gap; M. Trevisan & G. A. Mamon 2017).

5.3. AGN and Star Formation

One of our key results in Section 4.3 (Figure 8) is the connection of AGN to halo-integrated H I content and FSMGR. At low halo masses $M_{\rm halo} \lesssim 10^{12.1}\,M_{\odot}$, AGN-hosting halos show a broad valley in median $M_{\rm HI,grp}/M_{\rm halo}$ and median FSMGR_{grp} compared to non-AGN-hosting halos at fixed halo mass. The trend that non-AGN-hosting halos have higher median $M_{\rm HI,grp}/M_{\rm halo}$ and FSMGR_{grp} continues just past the bimodality scale to $M_{\rm halo} \sim 10^{12.3}\,M_{\odot}$, above which all of our halos host AGN. At higher masses, we find a possible valley at $M_{\rm halo} \sim 10^{13}\,M_{\odot}$, though whether it has a relationship to AGN is unknown. Interestingly, S. L. Ellison et al. (2019) found that the H I-richness of AGN-host galaxies is statistically lower than that of non-AGN hosts below galaxy $M_* \sim 10^{10.25}\,M_{\odot}$ (corresponding to $M_{\rm halo} = 10^{11.9}\,M_{\odot}$ central galaxies in ECO), with opposite behavior at higher stellar masses. In this section, we discuss possible scenarios that may account for these trends and features below, across, and above the bimodality scale.

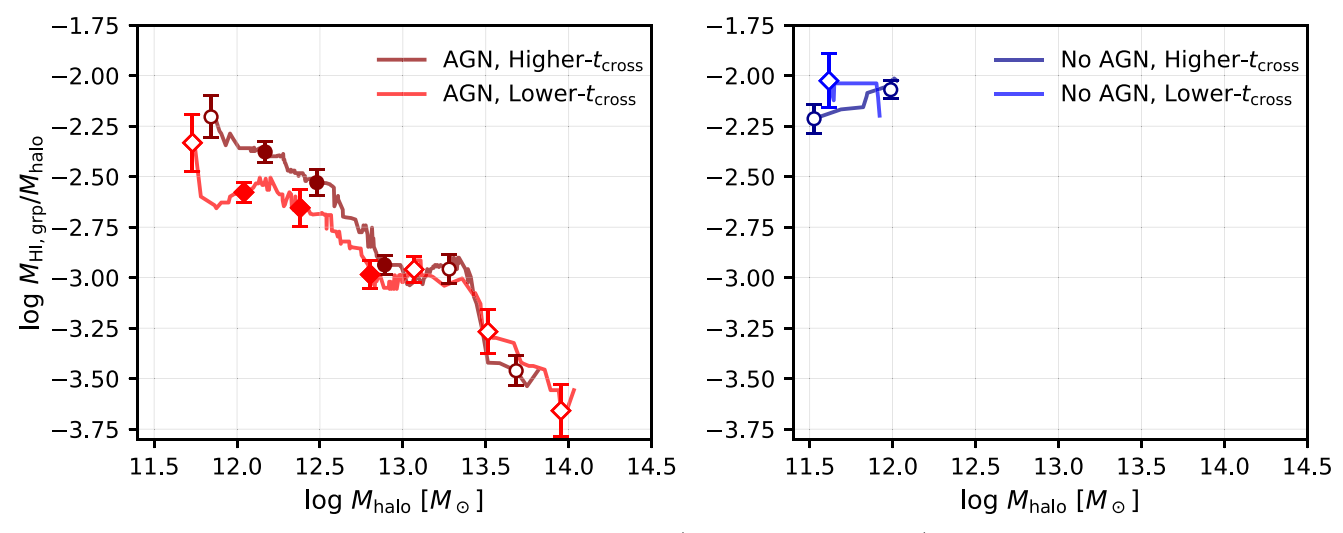


Figure 10. Demonstration of the independent effects of AGN and t_{cross} on $M_{HI,grp}/M_{halo}$. Left: median $M_{HI,grp}/M_{halo}$ vs. M_{halo} for higher- t_{cross} (thin line) and lower- t_{cross} (thick line) AGN-hosting halos. Lines, points, and error bars are as in Figure 8. $N_{galaxies} = 1$ halos are excluded. Right: same as the left panel, but for non-AGN-hosting halos.

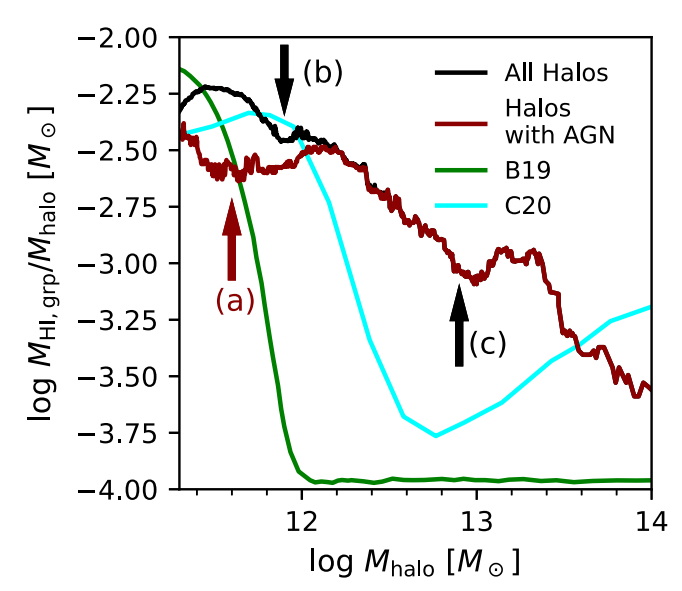


Figure 11. Observed $M_{\rm HL,grp}/M_{\rm halo}$ vs. $M_{\rm halo}$ compared to theoretical predictions. The black line represents the medians for G3 groups (excluding groups that lack a definite AGN-hosting or non-AGN-hosting classification), calculated in sliding windows as in Figure 8. The red line shows only AGN-hosting groups. The green and cyan lines show theoretical predictions from C. Baugh et al. (2019) and G. Chauhan et al. (2020), for which we have normalized their $M_{\rm HL,grp}/M_{\rm halo}$ relations to give $M_{\rm HL,grp}/M_{\rm halo}$ for AGN-hosting halos below the bimodality scale, (b) the narrower valley in $M_{\rm HL,grp}/M_{\rm halo}$ for all halos, and (c) a possible high-mass valley, as discussed in Section 5.3.

5.3.1. Below the Bimodality Scale

We consider two scenarios that may explain the valley in $M_{\rm HI,grp}/M_{\rm halo}$ and FSMGR_{grp} for AGN-hosting halos below the bimodality scale: (1) AGN feedback may suppress H I content and SF, and (2) a reduction in SF and associated feedback, perhaps for reasons unrelated to AGN fueling, may enable efficient gas inflow to fuel AGN activity or may simply enable AGN detection.

In scenario 1, AGN feedback may heat the halo gas or cause atomic gas blowout in galaxies, reducing the fuel supply for

SF. This scenario, gas heating specifically, is predicted by multiple semi-analytic models of the $M_{\rm HI,grp}$ – $M_{\rm halo}$ relation, which show a dip at $\log M_{\rm halo} = 10^{12} - 10^{12.5} M_{\odot}$ (H.-S. Kim et al. 2017; C. Baugh et al. 2019; G. Chauhan et al. 2020). Prior observational efforts including H23 have failed to detect a dip directly, a failure usually attributed to systematic errors in binning or halo mass estimation (G. Chauhan et al. 2021; A. Dev et al. 2023). In hindsight, a hint of a dip near $M_{\rm halo} \sim 10^{12} \, M_{\odot}$ was present in the combined G3 data set in H23 (their Figures 16 and 18). Figure 11 shows how this dip manifests in a plot of $M_{\rm HI,grp}/M_{\rm halo}$ versus $M_{\rm halo}$ along with two theoretical predictions. By comparing the lines for all halos and for AGN-hosting halos, Figure 11 shows that a shallow valley in the $M_{\rm HI,grp}/M_{\rm halo}$ versus $M_{\rm halo}$ relation across $M_{\rm halo} \sim 10^{11.8}\,M_{\odot}$ is caused by a deeper depression in the H I content of low-mass, AGN-hosting halos. Below the bimodality scale, this deeper valley is diluted by the large fraction of non-AGN-hosting halos, so the shallow valley becomes prominent as the fraction of AGN-hosting halos crosses $\sim 50\%$ around $M_{\rm halo} \sim 10^{11.7}\,M_{\odot}$ (see Figure 8). Figure 11 also shows that the C. Baugh et al. (2019) and G. Chauhan et al. (2020) semi-analytic models deviate substantially from this observed valley in $M_{\rm HI,grp}/M_{\rm halo}$, predicting much deeper and wider "troughs" at higher masses. The observed $M_{\rm halo} \sim 10^{11.8} \, M_{\odot}$ valley for all halos is much smaller, only ~0.1 dex deep, although it is much deeper for AGN-hosting halos taken alone, \sim 0.25 dex. In addition, the observed valley is located mostly below the bimodality scale, for both AGNhosting halos specifically and all halos (Figure 11). (We do also see structure in the relation near $M_{\rm halo} \sim 10^{13} \, M_{\odot}$, which could be a weaker valley similar to that of C20, as will be discussed in Section 5.3.2.) The failure of theoretical models to predict a valley below the bimodality scale suggests that these models are not yet realistically including low-metallicity and/or highly star-forming AGN populations such as composite galaxies and SF-AGN (AGN registering as AGN in the S. Veilleux & D. E. Osterbrock 1987 diagnostic plots but as SF in the J. A. Baldwin et al. 1981 BPT plot; M. S. Polimera et al. 2022). Composites and SF-AGN dominate the RESOLVE/ECO AGN

inventory up to the bimodality scale (M. S. Polimera et al. 2022; M. S. Polimera et al. 2025, in preparation).

In scenario 2, the suppressed H I content of AGN-hosting groups could reflect an inverted causality, wherein lower HI content and thus reduced SF feedback might allow gas to flow all the way to the black hole, as predicted especially for dwarf galaxies in some models (D. Anglés-Alcázar et al. 2017; M. Habouzit et al. 2017; M. Trebitsch et al. 2018). In observations, L. J. Latimer et al. (2019) have found that AGN are disproportionately uncommon in highly starbursting compact blue dwarfs (see also J. D. Bradford et al. 2018; S. J. Penny et al. 2018). Another version of scenario 2 is that reduced SF makes AGN easier to detect (M. S. Polimera et al. 2022). The black hole masses of dwarf AGN galaxies are expected to be $\sim 10^3 - 10^5 M_{\odot}$, so their optical AGN signatures can be diluted in the presence of the intense SF typical of $z \sim 0$ dwarf galaxies (A. E. Reines et al. 2020). This bias is reduced in the metallicity-insensitive S. Veilleux & D. E. Osterbrock (1987) diagnostic plots, which can identify AGN down to 8%– 16% AGN spectral contribution for a typical metal-poor dwarf (M. S. Polimera et al. 2022).

5.3.2. Above the Bimodality Scale

Above the bimodality scale, we see that the trend of higher median $M_{\rm HI,grp}/M_{\rm halo}$ and FSMGR_{grp} continues to $M_{\rm halo} \sim 10^{12.3} \, M_{\odot}$, above which non-AGN-hosting halos become nonexistent in our sample. Interestingly, we also find a possible high-mass valley for AGN-hosting halos near $M_{\rm halo} \sim 10^{13} \, M_{\odot}$ (see Figure 11). We leave open the interpretation of this apparent feature, but we note that, by analogy with the lower-mass valley, future work may benefit from examining whether the higher-mass feature is associated with any special subpopulations of AGN and their feedback properties. For example, a high-mass valley could hypothetically derive from a more prominent valley associated with halos hosting AGN in an efficient feedback mode that is diluted by other halos hosting AGN with less intense feedback. The AGN classifications used for our analysis are based on optical emission-line diagnostics and mid-IR photometry (M. S. Polimera et al. 2022; M. S. Polimera et al. 2025, in preparation), so we do not have the ability to test such a scenario. Since we lack systematic X-ray and radio AGN classifications, our AGN data will not fully reflect feedback from obscured or radio-loud AGN. Past work suggests that AGN feedback may operate in two modes of growth, "bright" and "radio" (R. S. Somerville et al. 2008; T. M. Heckman & P. N. Best 2014), both of which could influence halo H I content. In the bright mode, AGN may produce harsh radiation and winds that suppress accretion and SF. In the radio mode, relativistic jets may heat accreting gas and thereby counteract gas cooling. The numerical abundance of these AGN subtypes may vary with halo mass or galaxy stellar mass. For example, H. Miraghaei (2020) showed that the fractions of radio and optical AGN vary with both galaxy stellar mass and environment, considering both field versus group galaxies and central galaxies versus satellite galaxies. Thus, a careful assessment of AGN subtypes and their corresponding feedback modes would be needed to ascertain how our results relate to AGN feedback.

5.3.3. Across the Bimodality Scale

As mentioned, S. L. Ellison et al. (2019) have observed a reversal across the bimodality scale in whether AGN-hosting or

non-AGN-hosting galaxies have higher HI gas-to-stellar mass ratios. In particular, they found elevated H I content in massive AGN-hosting galaxies (10 $< \log M_* [M_{\odot}] < 10.8$) at fixed stellar mass. Our results do not show an analogous reversal. but we also lack any non-AGN-hosting halos above $M_{\rm halo}\sim 10^{12.3}\,M_{\odot}$, illustrating the difference between analyzing individual galaxies and analyzing entire halos. With halo mass increasing above the bimodality scale, galaxies increasingly reside in higher-richness multiple-galaxy groups, so non-AGN-hosting groups can be scarce even if there are still many individual non-AGN-hosting galaxies. In any case, the reversal S. L. Ellison et al. (2019) observed disappeared when the AGN and non-AGN samples were fixed in SF rate in addition to stellar mass. The authors argued that the original difference stemmed from the fact that, at fixed stellar mass, AGN preferentially reside in star-forming or green valley galaxies, which tend to have higher H I content. In our case, we have not replicated our Figure 8 analysis in fixed bins of M_{halo} and FSMGR_{grp} together, but we note that the similar behavior of the $M_{\rm HI,grp}/M_{\rm halo}$ and FSMGR_{grp} lines in Figure 8 is expected given the tight correlation between galaxy atomic gas-to-stellar mass ratio and FSMGR (S. J. Kannappan et al. 2013).

The question, then, is why AGN are more common in gasrich and star-forming galaxies. The simple explanation that cold gas fuels both SF and AGN seems incomplete, since below the bimodality scale AGN-hosting halos instead have lower H I content and FSMGR_{grp} than non-AGN-hosting halos. The reversal of this result across the bimodality scale could suggest a relationship to halo gas physics. In the theoretical model of G. Dashyan et al. (2018), there exists a critical halo mass $M_{\rm halo} \sim 10^{12} M_{\odot}$ (at $z \lesssim 1$) below which AGN can expel HI gas from dwarf galaxies, and observations have indeed found evidence for HI gas suppression in dwarf galaxy AGN hosts (e.g., J. D. Bradford et al. 2018). This ejective AGN feedback mode contrasts with the feedback mode that is theoretically expected for halos above the bimodality scale, in which the halo gas, having been shock-heated into a dilute medium, becomes more susceptible to radiative feedback from radio jets (A. Dekel & Y. Birnboim 2006). Understanding the galaxy mass and/or halo mass dependences of different modes of AGN feedback remains a key research question.

Since AGN feedback efficiency (see D. J. Croton et al. 2006) controls the location and depth of the dip in the predicted $M_{\rm HI}$, $_{\rm grp}$ – $M_{\rm halo}$ relation of G. Chauhan et al. (2020), such that higher AGN feedback efficiency corresponds to dips located at lower halo masses, the features we observe may help place constraints on the frequency and/or intensity of AGN feedback. The possibility that there are two valleys may imply different regimes of feedback mode and efficiency. We defer quantitative analysis of the location and depth of the valleys to future work. Even interpreting the more convincing $M_{\rm halo} \sim 10^{11.8} M_{\odot}$ valley in this context would require evaluation with mock catalogs since systematic group-finding and halo mass estimation errors affect the shape and scatter of the $M_{\rm HI,grp}$ – $M_{\rm halo}$ relation (K. D. Eckert et al. 2017; G. Chauhan et al. 2021; A. Dev et al. 2023; Z. L. Hutchens et al. 2023).

6. Conclusions

In this work, we have combined archival RASS X-ray observations with the highly complete and volume-limited RESOLVE and ECO surveys. Using these surveys' G3 group catalogs, comprehensive H I gas and SF data, and state-of-the-

art census of optical and mid-IR AGN (including the new SF-AGN category introduced by M. S. Polimera et al. 2022 that tracks dwarf AGN), we have examined the connection between group cold gas content and group X-ray emission as a function of halo mass, virialization state, SF, and AGN presence. Our key results can be summarized as follows:

- 1. We find that as halo mass increases, group H I content decreases while total X-ray emission and hot gas increase. Stacking RASS data, we detect hot gas in groups confidently at $M_{\rm halo}=10^{12.6}-10^{14}\,M_{\odot}$ and unambiguously at $M_{\rm halo}=10^{14}-10^{14.5}\,M_{\odot}$. We find that the X-ray emission from lower-mass halos can most likely be explained by AGN or XRBs, though we note that the estimation of XRB emission is a key area of uncertainty where future improvements can lead to better measurements of the group hot gas inventory (Section 5.1; Figures 3 and 4).
- 2. We identify a transition to increased spread in group gas content at fixed halo mass below $\log(t_{\rm cross}/13.8~{\rm Gyr}) = -0.86$, corresponding to $t_{\rm cross} \sim 2~{\rm Gyr}$. Defining lower- $t_{\rm cross}$ and higher- $t_{\rm cross}$ categories across this transition, we find that lower- $t_{\rm cross}$ groups show reduced median $M_{\rm HI}$, $_{\rm grp}/M_{\rm halo}$ compared to higher- $t_{\rm cross}$ groups at fixed halo mass. Above $M_{\rm halo} = 10^{13.3} M_{\odot}$, we additionally find increased X-ray emission for lower- $t_{\rm cross}$ groups. In contrast, we find enhanced X-ray emission for higher- $t_{\rm cross}$ groups at $M_{\rm halo} = 10^{12.6} 10^{13.3} M_{\odot}$. In this small-group regime, mergers and projection effects are expected to have a larger influence on $t_{\rm cross}$ (Sections 4.2 and 5.2; Figures 5–7).
- 3. Below the bimodality scale $(M_{\rm halo} = 10^{12.1} M_{\odot})$, halos with AGN exhibit a broad valley in FSMGR_{grp} and H I-to-halo mass ratio compared to non-AGN-hosting halos at fixed halo mass. We have argued that this result may be consistent with either of two physical scenarios: (1) gas heating or blowout from AGN removes H I and suppresses SF, or (2) reduced SF feedback enables H I inflow for AGN fueling, or reduced SF simply makes AGN easier to detect (Sections 4.3 and 5.3; Figures 8–10).
- 4. The trend of elevated H I-to-halo mass ratio and FSMGR_{grp} for non-AGN-hosting halos continues until such halos become nonexistent in our sample at $M_{\rm halo} \gtrsim 10^{12.3}\,M_{\odot}$, just above the bimodality scale. We also detect significant X-ray emission from AGN-hosting halos at $M_{\rm halo} = 10^{11.5} 10^{12.1}\,M_{\odot}$ and $M_{\rm halo} = 10^{12.1} 10^{12.6}\,M_{\odot}$. These results hold even if we treat all mid-IR AGN-host galaxies as non-AGN-hosting galaxies (Sections 4.3 and 5.3; Figures 8–10).
- 5. We find that AGN-hosting halos below and just above the bimodality scale show reduced FSMGR_{grp} at fixed halo mass compared to non-AGN-hosting halos. This pattern for FSMGR_{grp} matches that for H I content, as expected based on the tight relationship between galaxy FSMGR and galaxy H I-to-stellar mass ratio seen in S. J. Kannappan et al. (2013) (Sections 4.3 and 5.3; Figure 8).
- 6. Updating H23, we now report evidence for a dip in the $M_{\rm HI,grp}$ – $M_{\rm halo}$ relation (in hindsight evident in Figures 16 and 18 in H23). This dip coincides with a shallow valley in the median $M_{\rm HI,grp}/M_{\rm halo}$ versus $M_{\rm halo}$ relation across $M_{\rm halo} \sim 10^{11.8}\,M_{\odot}$ as the fraction of halos containing AGN crosses 50%, reflecting a deeper and wider valley in $M_{\rm HI,grp}/M_{\rm halo}$ for AGN-hosting halos below the

bimodality scale. While an AGN-feedback-driven dip in the $M_{\rm HI,grp}$ – $M_{\rm halo}$ relation has been theoretically predicted (H.-S. Kim et al. 2017; C. Baugh et al. 2019; G. Chauhan et al. 2020, 2021), these predicted dips correspond to much deeper $M_{\rm HI,grp}/M_{\rm halo}$ troughs at masses above the bimodality scale. The valley we have discovered is centered between the threshold and bimodality scales for all halos and is driven by an even broader valley that extends well into the dwarf regime for AGN-hosting halos. We do see a possible high-mass valley in the $M_{\rm HI,grp}/M_{\rm halo}$ versus $M_{\rm halo}$ relation near $M_{\rm halo} \sim 10^{13}\,M_{\odot}$. If it is a valley, it is much shallower than theory predicts, and its relationship to AGN or AGN subtype activity is unknown (Sections 4.3 and 5.3; Figures 8–11).

These results illustrate the wide variety of drivers of group HI content and group X-ray emission at fixed halo mass, thereby deepening our understanding of the rich scatter in the $M_{\rm HI,grp}$ - $M_{\rm halo}$ relation, which has only recently been quantified. While our work has clearly demonstrated the importance of virialization state, SF, and AGN presence in shaping the group gas inventory, it has also raised several interesting puzzles. Some unresolved questions include (a) the physical meaning of the $t_{\rm cross} \sim 2$ Gyr transition in group gas content, (b) the cause of the reversal of enhanced X-ray emission for lower- t_{cross} versus higher- t_{cross} groups across the shutdown scale, and (c) the physical drivers of reduced HI content in AGN-hosting halos, especially in relation to the newly discovered dip in the $M_{\rm HI,grp}$ - $M_{\rm halo}$ relation below the bimodality scale. Future work to address these puzzles will provide essential insights into how galaxies evolve in relation to their dark matter halos.

Acknowledgments

We are grateful for feedback from the anonymous reviewer that improved the quality and clarity of this work. We thank Mugdha Polimera, Andrew Mann, Adrienne Erickcek, Andreas Berlind, Ella Castelloe, Hannah Perkins, and Chris Richardson for helpful conversations at various stages of this work. We also thank Michael Corcoran and Koji Mukai for support using HEASARC software/data, including PIMMS. Z.L.H., S.J.K., and D.S.C. acknowledge support from NSF grants AST-1814486 and AST-2007351. Z.L.H. and D.S.C. are also grateful for support through North Carolina Space Grant Graduate Research Fellowships. K.M.H. acknowledges financial support from the grant CEX2021-001131-S funded by MCIN/AEI/ 10.13039/501100011033 from the coordination of the participation in SKA-SPAIN funded by the Ministry of Science and Innovation (MCIN) and from grant PID2021-123930OB-C21 funded by MCIN/AEI/ 10.13039/501100011033 by "ERDF A way of making Europe" and by the "European Union." A.J.B. acknowledges support from NSF grants AST-1814421 and AST-2308161 and from the Radcliffe Institute for Advanced Study at Harvard University. This work has made use of the RESOLVE survey, which is funded under NSF AST CAREER grant 0955368 (PI S. Kannappan). This research has made use of data and/or software provided by the High Energy Astrophysics Science Archive Research Center (HEASARC), which is a service of the Astrophysics Science Division at NASA/GSFC. This work made use of Astropy (http://www.astropy.org), a community-developed core Python package and an ecosystem of tools and resources for astronomy.

ORCID iDs

Zackary L. Hutchens https://orcid.org/0000-0002-8574-5495
Sheila J. Kannappan https://orcid.org/0000-0002-3378-6551
Kelley M. Hess https://orcid.org/0000-0001-9662-9089
Andrew J. Baker https://orcid.org/0000-0002-7892-396X
Ming Sun https://orcid.org/0000-0001-5880-0703
Kathleen D. Eckert https://orcid.org/0000-0002-1407-4700

References

```
Abadi, M. G., Moore, B., & Bower, R. G. 1999, MNRAS, 308, 947
Ai, M., & Zhu, M. 2018, ApJ, 862, 48
Anderson, M. E., Bregman, J. N., & Dai, X. 2012, ApJ, 762, 106
Anderson, M. E., Gaspari, M., White, S. D., Wang, W., & Dai, X. 2015,
       RAS, 449, 3806
Anglés-Alcázar, D., Davé, R., Faucher-Giguère, C.-A., Özel, F., &
   Hopkins, P. F. 2017, MNRAS, 464, 2840
Baldwin, J. A., Phillips, M. M., & Terlevich, R. 1981, PASP, 93, 5
Baugh, C., Gonzalez-Perez, V., Lagos, C. D., et al. 2019, MNRAS, 483, 4922
Behroozi, P. S., Conroy, C., & Wechsler, R. H. 2010, ApJ, 717, 379
Bekki, K., Couch, W. J., & Shioya, Y. 2002, ApJ, 577, 651
Birchall, K. L., Watson, M. G., Aird, J., & Starling, R. L. C. 2022, MNRAS,
Birnboim, Y., & Dekel, A. 2003, MNRAS, 345, 349
Blanton, M. R., & Berlind, A. A. 2007, ApJ, 664, 791
Boese, F. 2000, A&AS, 141, 507
Bogdán, Á., & Vogelsberger, M. 2022, in Handbook of X-Ray and Gamma-
   Ray Astrophysics, ed. C. Bambi & A. Santangelo (Berlin: Springer), 111
Boller, T., Freyberg, M., Trümper, J., et al. 2016, A&A, 588, A103
Boroson, B., Kim, D.-W., & Fabbiano, G. 2011, ApJ, 729, 12
Borthakur, S., Yun, M. S., Verdes-Montenegro, L., et al. 2015, ApJ, 812, 78
Bradford, J. D., Geha, M. C., Greene, J. E., Reines, A. E., & Dickey, C. M.
  2018, ApJ, 861, 50
Buat, V., Giovannoli, E., Takeuchi, T., et al. 2011, A&A, 529, A22
Carlberg, R., Yee, H., Morris, S., et al. 2001, ApJ, 563, 736
Cen, R., & Ostriker, J. P. 1999, ApJ, 514, 1
Chandrasekhar, S. 1943, ApJ, 97, 255
Chauhan, G., Lagos, C. d. P., Stevens, A. R., et al. 2020, MNRAS, 498, 44
Chauhan, G., Lagos, C. d. P., Stevens, A. R., et al. 2021, MNRAS, 506, 4893
Colbert, E. J., Heckman, T. M., Ptak, A. F., Strickland, D. K., & Weaver, K. A.
   2004, ApJ, 602, 231
Comerford, J. M., Pooley, D., Barrows, R. S., et al. 2015, ApJ, 806, 219
Croton, D. J., Springel, V., White, S. D., et al. 2006, MNRAS, 365, 11
Dai, X., Kochanek, C. S., & Morgan, N. D. 2007, ApJ, 658, 917
Dalcanton, J. J., Yoachim, P., & Bernstein, R. A. 2004, ApJ, 608, 189
Dashyan, G., Silk, J., Mamon, G. A., Dubois, Y., & Hartwig, T. 2018,
      IRAS, 473, 5698
Davé, R., Cen, R., Ostriker, J. P., et al. 2001, ApJ, 552, 473
David, L. P., Jones, C., Forman, W., Vargas, I. M., & Nulsen, P. 2006, ApJ,
   653, 207
De Grandi, S., Molendi, S., Böhringer, H., Chincarini, G., & Voges, W. 1997,
    ApJ, 486, 738
Dekel, A., & Birnboim, Y. 2006, MNRAS, 368, 2
Dekel, A., & Silk, J. 1986, ApJ, 303, 39
Desjardins, T. D., Gallagher, S. C., Hornschemeier, A. E., et al. 2014, ApJ,
Dev, A., Driver, S. P., Meyer, M., et al. 2023, MNRAS, 523, 2693
Di Matteo, P., Bournaud, F., Martig, M., et al. 2008, A&A, 492, 31
D'Onghia, E., Sommer-Larsen, J., Romeo, A., et al. 2005, ApJ, 630, L109
Dressler, A., & Shectman, S. A. 1988, AJ, 95, 985
Eckert, K. D., Kannappan, S. J., Lagos, C. d. P., et al. 2017, ApJ, 849, 20
Eckert, K. D., Kannappan, S. J., Stark, D. V., et al. 2015, ApJ, 810, 166
Eckert, K. D., Kannappan, S. J., Stark, D. V., et al. 2016, ApJ, 824, 124
Eckmiller, H., Hudson, D., & Reiprich, T. 2011, A&A, 535, A105
Ellison, S. L., Brown, T., Catinella, B., & Cortese, L. 2019, MNRAS,
Ferguson, H. C., & Sandage, A. 1990, AJ, 100, 1
Fielding, D., Quataert, E., McCourt, M., & Thompson, T. A. 2017, MNRAS,
Firth, P., Evstigneeva, E., Jones, J., et al. 2006, MNRAS, 372, 1856
Flesch, E. W. 2015, PASA, 32, e010
Forbes, D. A., Alabi, A., Romanowsky, A. J., et al. 2017, MNRAS, 464, L26
Gabor, J. M., & Davé, R. 2015, MNRAS, 447, 374
Gao, F., Wang, L., Pearson, W., et al. 2020, A&A, 637, A94
```

```
Garnett, D. R. 2002, ApJ, 581, 1019
Gaspari, M., Brighenti, F., Temi, P., & Ettori, S. 2014, ApJL, 783, L10
Gott, J. R., III, & Turner, E. L. 1977, ApJ, 213, 309
Goulding, A. D., Greene, J. E., Ma, C.-P., et al. 2016, ApJ, 826, 167
Gozaliasl, G., Finoguenov, A., Tanaka, M., et al. 2019, MNRAS, 483, 3545
Grcevich, J., & Putman, M. E. 2009, ApJ, 696, 385
Guo, H., Jones, M. G., Haynes, M. P., & Fu, J. 2020, ApJ, 894, 92
Habouzit, M., Volonteri, M., & Dubois, Y. 2017, MNRAS, 468, 3935
Hainline, K. N., Reines, A. E., Greene, J. E., & Stern, D. 2016, ApJ, 832, 119
Haynes, M. P., Giovanelli, R., Kent, B. R., et al. 2018, ApJ, 861, 49
Haynes, M. P., Giovanelli, R., Martin, A. M., et al. 2011, AJ, 142, 170
Heckman, T. M., & Best, P. N. 2014, ARA&A, 52, 589
Hess, K. M., & Wilcots, E. M. 2013, AJ, 146, 124
Hickson, P., Mendes de Oliveira, C., Huchra, J. P., & Palumbo, G. G. 1992,
    ApJ, 399, 353
Hu, W., & Kravtsov, A. V. 2003, ApJ, 584, 702
Hutchens, Z. L., Kannappan, S. J., Berlind, A. A., et al. 2023, ApJ, 956, 51
Jakobs, A., Viola, M., McCarthy, I., et al. 2018, MNRAS, 480, 3338
Jones, M. G., Sand, D. J., Karunakaran, A., et al. 2024, ApJ, 966, 93
Kalberla, P. M., Burton, W., Hartmann, D., et al. 2005, A&A, 440, 775
Kalberla, P. M., & Kerp, J. 2009, ARA&A, 47, 27
Kannappan, S. J. 2004, ApJ, 611, L89
Kannappan, S. J., & Gawiser, E. 2007, ApJ, 657, L5
Kannappan, S. J., Guie, J. M., & Baker, A. J. 2009, AJ, 138, 579
Kannappan, S. J., Stark, D. V., Eckert, K. D., et al. 2013, ApJ, 777, 42
Kannappan, S. J., & Wei, L. H. 2008, in AIP Conference Proceedings 1035,
   The Evolution of Galaxies Through the Neutral Hydrogen Window
  (Melville, NY: AIP), 163
Kauffmann, G., Heckman, T. M., White, S. D. M., et al. 2003, MNRAS,
  341, 54
Kaviraj, S. 2014, MNRAS, 440, 2944
Kereš, D., Katz, N., Weinberg, D. H., & Davé, R. 2005, MNRAS, 363, 2
Kim, D.-W., & Fabbiano, G. 2013, ApJ, 776, 116
Kim, H.-S., Wyithe, J. S. B., Baugh, C. M., et al. 2017, MNRAS, 465, 111
Kravtsov, A. V., Berlind, A. A., Wechsler, R. H., et al. 2004, ApJ, 609, 35
Latimer, L. J., Reines, A. E., Plotkin, R. M., Russell, T. D., & Condon, J. J.
  2019, ApJ, 884, 78
Lehmer, B., Alexander, D., Bauer, F., et al. 2010, ApJ, 724, 559
Lehmer, B. D., Eufrasio, R. T., Basu-Zych, A., et al. 2022, ApJ, 930, 135
Lehmer, B. D., Eufrasio, R. T., Tzanavaris, P., et al. 2019, ApJS, 243, 3
Lehmer, B. D., Ferrell, A. P., Doore, K., et al. 2020, ApJS, 248, 31
Lehmer, B. D., Monson, E. B., Eufrasio, R. T., et al. 2024, ApJ, 977, 189
Li, T., Simon, J. D., Drlica-Wagner, A., et al. 2017, ApJ, 838, 8
Liu, H.-Y., Liu, W.-J., Dong, X.-B., et al. 2019, ApJS, 243, 21
Lower, S., Narayanan, D., Leja, J., et al. 2020, ApJ, 904, 33
Mezcua, M., & Sánchez, H. D. 2024, MNRAS, 528, 5252
Mineo, S., Gilfanov, M., Lehmer, B. D., Morrison, G. E., & Sunyaev, R. 2014,
   MNRAS, 437, 1698
Mineo, S., Gilfanov, M., & Sunyaev, R. 2012, MNRAS, 419, 2095
Miraghaei, H. 2020, AJ, 160, 227
Moffett, A. J., Kannappan, S. J., Berlind, A. A., et al. 2015, ApJ, 812, 89
Mukai, K. 1993, Legac, 3, 21
Mulchaey, J. S. 2000, ARA&A, 38, 289
Nelson, D., Vogelsberger, M., Genel, S., et al. 2013, MNRAS, 429, 3353
Obuljen, A., Alonso, D., Villaescusa-Navarro, F., Yoon, I., & Jones, M. 2019,
       RAS, 486, 5124
O'Sullivan, E., Kolokythas, K., Kantharia, N. G., et al. 2018, MNRAS,
  473, 5248
Penny, S. J., Masters, K. L., Smethurst, R., et al. 2018, MNRAS, 476, 979
Pipino, A., Cibinel, A., Tacchella, S., et al. 2014, ApJ, 797, 127
Polimera, M. S., Kannappan, S. J., Richardson, C. T., et al. 2022, ApJ, 931, 44
Ponman, T., Allan, D., Jones, L., et al. 1994, Natur, 369, 462
Price-Whelan, A. M., Lim, P. L., Earl, N., et al. 2022, ApJ, 935, 167
Putman, M. E., Zheng, Y., Price-Whelan, A. M., et al. 2021, ApJ, 913, 53
Ranalli, P., Comastri, A., & Setti, G. 2003, A&A, 399, 39
Rasmussen, J., Bai, X.-N., Mulchaey, J. S., et al. 2012, ApJ, 747, 31
Reines, A. E., Condon, J. J., Darling, J., & Greene, J. E. 2020, ApJ, 888, 36
Rood, H. J., & Dickel, J. R. 1978, ApJ, 224, 724
Saraf, M., Cortese, L., Wong, O. I., et al. 2024, MNRAS, 530, 2420
Satyapal, S., Abel, N. P., & Secrest, N. J. 2018, ApJ, 858, 38
Shi, X., Nagai, D., Aung, H., & Wetzel, A. 2020, MNRAS, 495, 784
Sinha, M., & Holley-Bockelmann, K. 2009, MNRAS, 397, 190
Skibba, R. A., van den Bosch, F. C., Yang, X., et al. 2011, MNRAS, 410,
Smith, B. D., Hallman, E. J., Shull, J. M., & O'Shea, B. W. 2011, ApJ, 731, 6
Snowden, S., McCammon, D., Burrows, D., & Mendenhall, J. 1994, ApJ,
  424, 714
```

```
Somerville, R. S., Hopkins, P. F., Cox, T. J., Robertson, B. E., & Hernquist, L. 2008, MNRAS, 391, 481
```

Springob, C. M., Haynes, M. P., Giovanelli, R., & Kent, B. R. 2005, ApJS, 160, 149

Stark, D. V., Kannappan, S. J., Eckert, K. D., et al. 2016, ApJ, 832, 126

Stark, D. V., Kannappan, S. J., Wei, L. H., et al. 2013, ApJ, 769, 82

Stasińska, G., Cid Fernandes, R., Mateus, A., Sodré, L., & Asari, N. V. 2006, MNRAS, 371, 972

Sturm, M. R., Hayes, B., & Reines, A. E. 2025, arXiv:2501.09791 Sun, M., Voit, G., Donahue, M., et al. 2009, ApJ, 693, 1142 Tinker, J., Kravtsov, A. V., Klypin, A., et al. 2008, ApJ, 688, 709

Trebitsch, M., Volonteri, M., Dubois, Y., & Madau, P. 2018, MNRAS, 478, 5607

Trevisan, M., & Mamon, G. A. 2017, MNRAS, 471, 2022

Van Driel, W., Augarde, R., Bottinelli, L., et al. 1992, A&A, 259, 71

Veilleux, S., & Osterbrock, D. E. 1987, ApJS, 63, 295

Véron-Cetty, M. P., & Véron, P. 2006, A&A, 455, 773

Voges, W. 1993, AdSpR, 13, 391

Voges, W., Aschenbach, B., Boller, T., et al. 1999, A&A, 349, 389

Wilcots, E. M. 2009, AN, 330, 1059

Zhang, Y., Comparat, J., Ponti, G., et al. 2024, A&A, 690, A268

Zhu, J., & Putman, M. E. 2023, MNRAS, 521, 3765